J. Fluid Mech. (2003), *vol.* 492, *pp.* 101–129.
DOI: 10.1017/S0022112003005652 Printed in the United Kingdom

Interaction of sedimenting spheres with multiple surface roughness scales

By YU ZHAO AND ROBERT H. DAVIS†

Department of Chemical Engineering, University of Colorado, Boulder, CO 80309-0424, USA

(Received 9 July 2002 and in revised form 25 April 2003)

The interaction of a pair of spherical particles of different densities and/or sizes with microscopic surface roughness sedimenting due to gravity in a viscous fluid is analysed by theory and experiment. The surface topography is modelled as a combination of small uniformly distributed bumps of uniform height and larger bumps that are more sparsely distributed. The existence of these surface asperities allows the spheres to physically contact each other, so that both hydrodynamic and solid-contact forces are important. When the angle between the line of centres and vertical is small, the spheres may rotate as a rigid body because they are not able to roll up and over a large bump. As this angle increases, however, the heavy sphere rolls and slips past the lighter sphere, and the separation between the nominal surfaces of the spheres varies between the heights of the small and large asperities. When considering many encounters, there is a distribution of nominal separations at each angle due to the distribution of initial conditions and surface topography. The average nominal separation generally increases with increasing angle between the line of centres and vertical because the normal component of gravity, which drives the spheres close together after an encounter with a large bump lifts them apart, decreases as this angle increases.

1. Introduction

The behaviour of non-colloidal particles suspended in a viscous fluid at low Reynolds numbers is of great interest to many branches of technology. While lubrication forces prevent contact of perfectly smooth particles in a continuum fluid under the action of a finite force (Reynolds 1886), real particles in a viscous fluid can make direct solid–solid contacts due to their microscopic surface roughness.

The existence of contact forces has caused many experiments to exhibit results which differ from theoretical predictions for smooth spheres. In the case of shear flow, it was found that the particles may rotate as a pair when in contact, and then separate (Arp & Mason 1977). Furthermore, Parsi & Gadala-Maria (1987) found that the pair-distribution function for sheared suspensions is higher on the approaching side of a reference sphere than on the receding side, and Rampall, Smart & Leighton (1997) presented further evidence that contact forces break the fore-and-aft symmetry predicted for sheared suspensions of smooth spheres. In sedimentation, Zeng, Kerns & Davis (1996) and Zhao & Davis (2002) also showed that the relative trajectory of two unequal spheres loses the fore-and-aft symmetry predicted for smooth spheres, when contact occurs due to microscopic surface roughness.

† Author to whom correspondence should be addressed: robert.davis@colorado.edu

To describe the interaction of contacting particle pairs in a dilute suspension, Davis (1992) proposed two models: the stick/rotate model, where the spheres lock together and rotate like a rigid body, as observed by Arp & Mason (1977) in a shear flow, and the roll/slip model, where one sphere rolls with or without slipping around the surface of the other, as observed by Zeng *et al.* (1996) and Zhao & Davis (2002) for sedimenting particles. In both models, the contact forces are assumed to be compressive but not tensile, so that relative motion along the line of centres is prevented by contact when the spheres are pushed together but not when they are pulled apart.

The presence of hydrodynamic surface roughness and the irreversible nature of the contact forces affect the rheological properties of suspensions. For example, Davis (1992) and da Cunha & Hinch (1996) examined the effects of pairwise contact interactions on hydrodynamic diffusion in dilute suspensions. Wilson & Davis (2000, 2002) calculated the effective viscosity and normal stress differences in dilute and concentrated suspensions of rough spheres during simple shear flow by using the roll/slip model to describe the pairwise interactions of particles in contact.

In related work, a rough sphere moving down an inclined plane was examined by Smart, Beimfohr & Leighton (1993) and Prokunin (1998), who considered a single scale of surface roughness. Galvin, Zhao & Davis (2001) and Zhao, Galvin & Davis (2002) subsequently explored multiple roughness scales by considering the sphere or plane to be covered by bumps of two different sizes. A key finding is that the average separation between the nominal surface of the sphere and plane increases with increasing inclination of the plane from horizontal, with the smaller bumps being most important at small angles and the larger bumps most important at large angles, as suggested previously by King & Leighton (1997).

In this paper, we consider gravitational interaction of two unequal spheres with multiple scales of microscopic bumps on the surface of one of the spheres. There is a low coverage of large bumps which are well separated by a higher coverage of small bumps. We are particularly interested in the average separation between the nominal surfaces of the two spheres as they move around each other, because this separation is expected to influence the rheological properties of suspensions. In § 2, a physical model is provided to describe the behaviour of two spheres experiencing both hydrodynamic and solid–solid interactions. In § 3, the experimental materials and method are described. In the next section, a discussion of the model results is presented, and then these results are compared with those from the experiments in § 5. Concluding remarks are given in § 6.

2. Theoretical development

Consider the motion of two unequal solid spheres of radii a_1 and a_2 and densities ρ_1 and ρ_2 falling due to gravity at low Reynolds number through a viscous fluid of viscosity μ and large extent. The spheres are large enough that Brownian motion and colloidal forces are negligible, but they are small enough that inertia is not important. Sphere 1 has a higher terminal velocity (due to its greater density and/or size) and falls past sphere 2. If the initial horizontal offset is sufficiently small, then the surfaces of the spheres may make physical contact due to microscopic surface roughness. As shown in figure 1, the microscopic roughness is assumed to reside on the heavy sphere and to be characterized by a combination of large bumps of height $\delta_L \ll \min(a_1, a_2)$ and small bumps with height $\delta_S < \delta_L$. The large bumps are assumed to be very sparse, so that they are encountered individually; they may have a distribution of heights, but

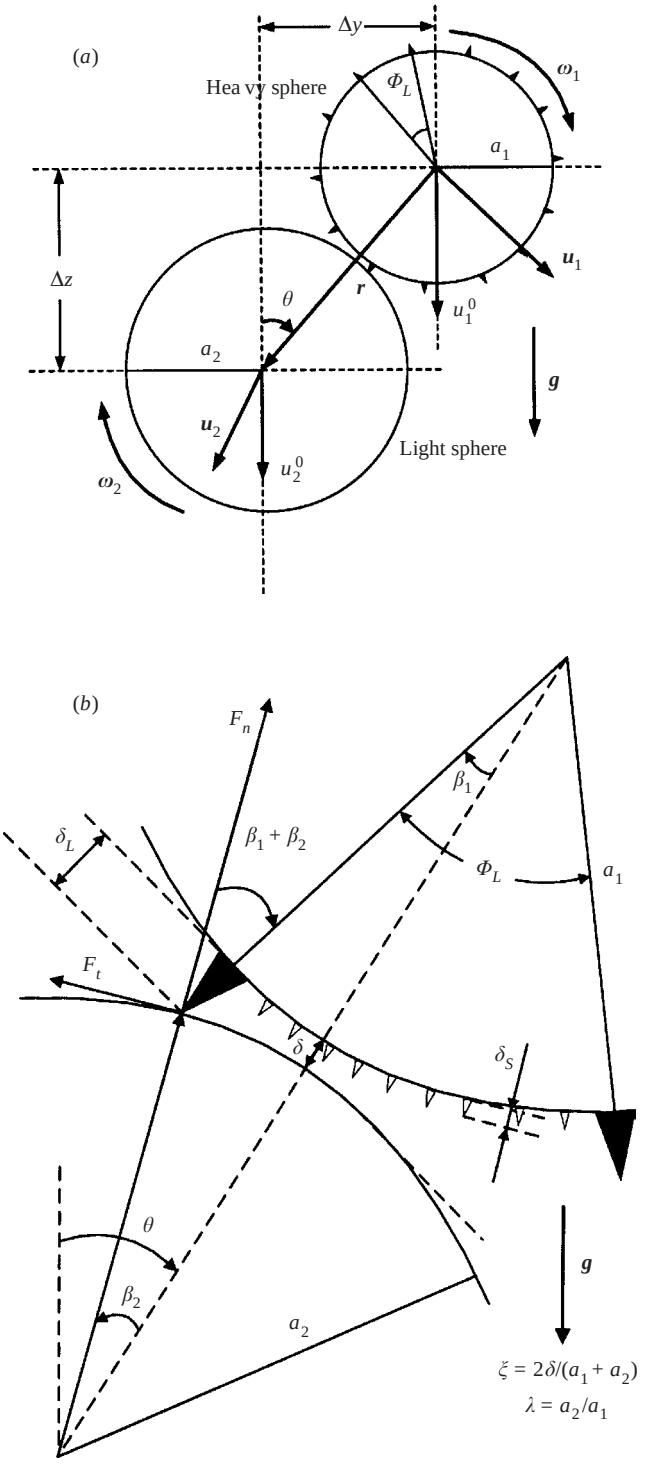

FIGURE 1. Coordinate system and sketch of (*a*) two interacting spheres and (*b*) close-up of contact interaction.

for simplicity we primarily consider large bumps of a single height. The separation between the nominal surfaces of the two spheres varies as they roll up and over the contact point on a large bump. In contrast, the small bumps have a somewhat higher surface coverage and keep the nominal surfaces at nearly constant separation δ_S when in contact on the small bumps. Depending on the initial orientation of the heavy sphere, contact may first occur on a large bump or on the small bumps.

Let θ be the angle between the line of centres and the gravity vector, with $\theta = \theta_0$ when contact first occurs at $t = t_0$. Further, let β_1 be the angle between the line of centres and the line joining the centre of the heavy sphere with the closest large bump at the time of contact, with $\beta_1 = \beta_0$ when contact first occurs. The rate of change of the angle $\beta_1(t)$ plays a key role in the progression of the two-sphere interaction after contact occurs. Its variation is given by

$$\frac{\mathrm{d}\beta_1}{\mathrm{d}t} = \omega_1 - \omega, \tag{2.1}$$

where ω_1 is the (clockwise) rotational rate of the heavy sphere and $\omega = \mathrm{d}\theta/\mathrm{d}t$ is the rotational rate of the line centres. For equal-size spheres, ω is usually larger than ω_1 (several special cases are discussed later), which leads to $\mathrm{d}\beta_1/\mathrm{d}t < 0$, indicating that the second large bump to be encountered is located clockwise from the first large bump.

The translational ($\boldsymbol{u}_1$ and $\boldsymbol{u}_2$) and rotational ($\boldsymbol{\omega}_1$ and $\boldsymbol{\omega}_2$) velocities of two spherical particles in response to the applied forces ($\boldsymbol{F}_1$ and $\boldsymbol{F}_2$) and torques ($\boldsymbol{L}_1$ and $\boldsymbol{L}_2$) may be written as linear superpositions for viscous interactions at low Reynolds number (Jeffrey & Onishi 1984):

$$\boldsymbol{u}_1 = \frac{\boldsymbol{F}_1}{6\pi\mu a_1}\cdot\left[x_{11}^a \boldsymbol{e}_r\boldsymbol{e}_r + y_{11}^a(\boldsymbol{I}-\boldsymbol{e}_r\boldsymbol{e}_r)\right] + \frac{\boldsymbol{F}_2}{3\pi\mu(a_1+a_2)}\cdot\left[x_{12}^a \boldsymbol{e}_r\boldsymbol{e}_r + y_{12}^a(\boldsymbol{I}-\boldsymbol{e}_r\boldsymbol{e}_r)\right] - \frac{y_{11}^b \boldsymbol{L}_1\times\boldsymbol{e}_r}{4\pi\mu a_1^2} - \frac{y_{21}^b \boldsymbol{L}_2\times\boldsymbol{e}_r}{\pi\mu(a_1+a_2)^2}, \tag{2.2}$$

$$\boldsymbol{u}_2 = \frac{\boldsymbol{F}_1}{3\pi\mu(a_1+a_2)}\cdot\left[x_{21}^a \boldsymbol{e}_r\boldsymbol{e}_r + y_{21}^a(\boldsymbol{I}-\boldsymbol{e}_r\boldsymbol{e}_r)\right] + \frac{\boldsymbol{F}_2}{6\pi\mu a_2}\cdot\left[x_{22}^a \boldsymbol{e}_r\boldsymbol{e}_r + y_{22}^a(\boldsymbol{I}-\boldsymbol{e}_r\boldsymbol{e}_r)\right] - \frac{y_{12}^b \boldsymbol{L}_1\times\boldsymbol{e}_r}{\pi\mu(a_1+a_2)^2} - \frac{y_{22}^b \boldsymbol{L}_2\times\boldsymbol{e}_r}{4\pi\mu a_2^2}, \tag{2.3}$$

$$\boldsymbol{\omega}_1 = \frac{y_{11}^b \boldsymbol{F}_1\times\boldsymbol{e}_r}{4\pi\mu a_1^2} + \frac{y_{12}^b \boldsymbol{F}_2\times\boldsymbol{e}_r}{\pi\mu(a_1+a_2)^2} + \frac{\boldsymbol{L}_1}{8\pi\mu a_1^3}\cdot\left[x_{11}^c \boldsymbol{e}_r\boldsymbol{e}_r + y_{11}^c(\boldsymbol{I}-\boldsymbol{e}_r\boldsymbol{e}_r)\right] + \frac{\boldsymbol{L}_2}{\pi\mu(a_1+a_2)^3}\cdot\left[x_{12}^c \boldsymbol{e}_r\boldsymbol{e}_r + y_{12}^c(\boldsymbol{I}-\boldsymbol{e}_r\boldsymbol{e}_r)\right], \tag{2.4}$$

$$\boldsymbol{\omega}_2 = \frac{y_{21}^b \boldsymbol{F}_1\times\boldsymbol{e}_r}{\pi\mu(a_1+a_2)^2} + \frac{y_{22}^b \boldsymbol{F}_2\times\boldsymbol{e}_r}{4\pi\mu a_2^2} + \frac{\boldsymbol{L}_1}{\pi\mu(a_1+a_2)^3}\cdot\left[x_{21}^c \boldsymbol{e}_r\boldsymbol{e}_r + y_{21}^c(\boldsymbol{I}-\boldsymbol{e}_r\boldsymbol{e}_r)\right] + \frac{\boldsymbol{L}_2}{8\pi\mu a_2^3}\cdot\left[x_{22}^c \boldsymbol{e}_r\boldsymbol{e}_r + y_{22}^c(\boldsymbol{I}-\boldsymbol{e}_r\boldsymbol{e}_r)\right], \tag{2.5}$$

where $\boldsymbol{e}_r = \boldsymbol{r}/r$ is the unit vector along the line of centres, $\boldsymbol{r}$ is centre-to-centre vector of magnitude r, $\boldsymbol{I}$ is the unit second-order tensor, and the x- and y-coefficients are dimensionless two-sphere mobility functions which depend only on the size ratio $\lambda = a_2/a_1$ and the dimensionless centre-to-centre separation $s = 2r/(a_1+a_2)$. The two-sphere mobility functions are expected to be valid, despite the presence of microscopic surface roughness, provided that the nominal surface-to-surface separation is large

compared to the roughness heights or the fractional coverage by bumps is small compared to unity (Smart & Leighton 1989). The applied forces and torques, and the resulting motion, depend on whether the spheres are touching on the large or small bumps, or not at all, as considered in the following subsections.

2.1. *Motion without contact*

When the two spheres are not in physical contact, which may occur prior to first contact or after contact with a large bump ends, the only applied forces are the net gravitational forces:

$$\boldsymbol{F}_1^g = \tfrac{4}{3}\pi a_1^3(\rho_1 - \rho)\boldsymbol{g} = 6\pi\mu a_1 \boldsymbol{u}_1^0, \tag{2.6}$$

$$\boldsymbol{F}_2^g = \tfrac{4}{3}\pi a_2^3(\rho_2 - \rho)\boldsymbol{g} = 6\pi\mu a_2 \boldsymbol{u}_2^0, \tag{2.7}$$

where ρ is the fluid density, $\boldsymbol{g}$ is the gravitational acceleration, and $\boldsymbol{u}_1^0$ and $\boldsymbol{u}_2^0$ are the Stokes settling velocities of the individual spheres when isolated. There are no applied torques in this case. Then, inserting (2.6) and (2.7) in (2.2)–(2.5) yields

$$\boldsymbol{u}_1 = u_1^0 \cos\theta \left(x_{11}^a + x_{12}^a \frac{2\lambda^3\gamma}{1+\gamma} \right) \boldsymbol{e}_r + u_1^0 \sin\theta \left(y_{11}^a + y_{12}^a \frac{2\lambda^3\gamma}{1+\lambda} \right) \boldsymbol{e}_\theta, \tag{2.8}$$

$$\boldsymbol{u}_2 = u_1^0 \cos\theta \left(\frac{2}{1+\lambda} x_{21}^a + \lambda^2\gamma x_{22}^a \right) \boldsymbol{e}_r + u_1^0 \sin\theta \left(\frac{2}{1+\lambda} y_{21}^a + \lambda^2\gamma y_{22}^a \right) \boldsymbol{e}_\theta, \tag{2.9}$$

$$\boldsymbol{\omega}_1 = \frac{u_1^0 \sin\theta}{a_1} \left(\tfrac{3}{2} y_{11}^b + y_{12}^b \frac{6\lambda^3\gamma}{(1+\lambda)^2} \right) \boldsymbol{e}_\phi, \tag{2.10}$$

$$\boldsymbol{\omega}_2 = \frac{u_1^0 \sin\theta}{a_1} \left(\frac{6}{(1+\lambda)^2} y_{21}^b + \tfrac{3}{2}\lambda\gamma y_{22}^b \right) \boldsymbol{e}_\phi, \tag{2.11}$$

where $\boldsymbol{e}_\theta$ is the unit vector in the direction of increasing θ, $\boldsymbol{e}_\phi = \boldsymbol{e}_\theta \times \boldsymbol{e}_r$, and $\gamma = (\rho_2 - \rho)/(\rho_1 - \rho)$.

It is common to examine the relative translational velocity of two sedimenting spheres (Batchelor & Wen 1982):

$$\frac{\mathrm{d}\boldsymbol{r}}{\mathrm{d}t} = \boldsymbol{u}_2 - \boldsymbol{u}_1 = \left(\boldsymbol{u}_2^0 - \boldsymbol{u}_1^0\right) \cdot \left(L\boldsymbol{e}_r\boldsymbol{e}_r + M(\boldsymbol{I} - \boldsymbol{e}_r\boldsymbol{e}_r)\right), \tag{2.12}$$

where the two-sphere relative mobility functions along and normal to the line of centres, respectively, are

$$L = \left(x_{11}^a - \frac{2(1-\lambda^3\gamma)}{1+\lambda} x_{12}^a - \lambda^2\gamma x_{22}^a \right) \Big/ (1 - \lambda^2\gamma), \tag{2.13}$$

$$M = \left(y_{11}^a - \frac{2(1-\lambda^3\gamma)}{1+\lambda} y_{12}^a - \lambda^2\gamma y_{22}^a \right) \Big/ (1 - \lambda^2\gamma), \tag{2.14}$$

using the identities $x_{21}^a = x_{12}^a$ and $y_{21}^a = y_{12}^a$. The rotational velocity of the line of centres is

$$\boldsymbol{\omega} = \omega\boldsymbol{e}_\phi = \frac{u_1^0 \sin\theta}{a_1} \left(\frac{2(1-\lambda^2\gamma)M}{(1+\lambda)s} \right) \boldsymbol{e}_\phi, \tag{2.15}$$

as follows from (2.12) and the kinematic relation $r\omega = (\boldsymbol{u}_1 - \boldsymbol{u}_2) \cdot \boldsymbol{e}_\theta$.

We restrict our attention to surface roughness elements which are sufficiently small and well spaced that they do not significantly modify the mobility functions of smooth

spheres, except when contact occurs (Smart & Leighton 1989). Then, the relative hydrodynamic mobility functions for non-touching spheres in near contact have the limiting forms (Jeffrey & Onishi 1984)

$$L = L_1\xi + O(\xi^2 \ln \xi^{-1}), \tag{2.16}$$

$$M = \frac{M_0(\ln \xi^{-1})^2 + M_1 \ln \xi^{-1} + M_2}{(\ln \xi^{-1})^2 + e_1 \ln \xi^{-1} + e_2}, \tag{2.17}$$

where the constants L_1, M_0, M_1, e_1 and e_2 depend only on λ and γ, and $\xi = 2\delta/(a_1 + a_2) = s - 2$ is the dimensionless separation between the nominal sphere surfaces.

When the spheres are close but not touching, then the normal component of their relative motion toward one another is resisted by a lubrication force of magnitude (Reynolds 1886)

$$F_L = \frac{-6\pi\mu a^2(\boldsymbol{u}_2 - \boldsymbol{u}_1)\cdot \boldsymbol{e}_r}{\delta} = \frac{-6\pi\mu a^2}{\delta}\frac{\mathrm{d}\delta}{\mathrm{d}t}, \tag{2.18}$$

where $a = a_1a_2/(a_1 + a_2)$ is the reduced radius. As written, this force is positive when the nominal separation δ is decreasing, and it acts in the positive $\boldsymbol{e}_r$-direction on sphere 2 and in the opposing direction on sphere 1. It is part of the hydrodynamic forces on the two spheres and balances the rest of the hydrodynamic forces (i.e. the drag forces on the falling particle pair away from the near-contact region) and the applied gravitational forces. Combining (2.12), (2.16) and (2.18) gives

$$F_L = \frac{12\pi\mu a_1 u_1^0 \lambda^2(1 - \lambda^2\gamma)L_1 \cos\theta}{(1 + \lambda)^3}. \tag{2.19}$$

2.2. *Contact with a large bump*

When a bump on the heavy sphere makes contact with the relatively smooth surface of the light sphere, then an equal and opposite contact force is exerted between the two spheres. The contact force includes a compressive component (F_n) that acts normal to the contact surface and a frictional component (F_t) that acts tangent to the contact surface. These forces on the heavy sphere are shown schematically in figure 1(*b*) for contact involving a single large bump; note that the direction of F_n is that of the outward normal to the surface of the smooth sphere and at angle β_2 to the line of centres, where geometrical constraints require that

$$a_2 \sin\beta_2 = (a_1 + \delta_L)\sin\beta_1 \quad \text{or} \quad \beta_2 \approx \beta_1/\lambda. \tag{2.20}$$

For simplicity we consider only large bumps that are located on or near the equator of the heavy sphere, so that the motion of the sphere centres remains in a single vertical plane. Then, the applied forces consisting of gravitational and contact forces on the two spheres are

$$\boldsymbol{F}_1 = \left(F_1^g \cos\theta - F_n \cos\beta_2 + F_t \sin\beta_2\right)\boldsymbol{e}_r + \left(F_1^g \sin\theta - F_n \sin\beta_2 - F_t \cos\beta_2\right)\boldsymbol{e}_\theta, \tag{2.21}$$

$$\boldsymbol{F}_2 = \left(F_2^g \cos\theta + F_n \cos\beta_2 - F_t \sin\beta_2\right)\boldsymbol{e}_r + \left(F_2^g \sin\theta + F_n \sin\beta_2 + F_t \cos\beta_2\right)\boldsymbol{e}_\theta. \tag{2.22}$$

The contact forces also result in applied torques about the sphere centres:

$$\boldsymbol{L}_1 = (a_1 + \delta_L)(F_n \sin(\beta_1 + \beta_2) + F_t \cos(\beta_1 + \beta_2))\boldsymbol{e}_\phi, \tag{2.23}$$

$$\boldsymbol{L}_2 = a_2 F_t \boldsymbol{e}_\phi. \tag{2.24}$$

Using (2.20)–(2.24) in (2.2)–(2.5) and employing the approximations $\delta_L \ll a_1$, $\cos\beta_2 \approx 1$, $\cos(\beta_1+\beta_2)\approx 1$, $\sin\beta_2 \approx \beta_2$ and $\sin(\beta_1+\beta_2)\approx(1+\lambda)\beta_2$ yields

$$\begin{aligned}
\boldsymbol{u}_1 \approx{}& u_1^0\cos\theta\left(x_{11}^a + x_{12}^a\frac{2\lambda^3\gamma}{1+\lambda}\right)\boldsymbol{e}_r + u_1^0\sin\theta\left(y_{11}^a + y_{12}^a\frac{2\lambda^3\gamma}{1+\lambda}\right)\boldsymbol{e}_\theta\\
&+\frac{F_t}{6\pi\mu a_1}\left(-y_{11}+\frac{2}{1+\lambda}y_{12}^a+\tfrac{3}{2}y_{11}^b+\frac{6\lambda}{(1+\lambda)^2}y_{21}^b\right)\boldsymbol{e}_\theta\\
&+\frac{\beta_1 F_n}{6\pi\mu a_1\lambda}\left(-y_{11}^a+\frac{2}{1+\lambda}y_{12}^a+\tfrac{3}{2}(1+\lambda)y_{11}^b\right)\boldsymbol{e}_\theta, \qquad (2.25)\\
\boldsymbol{u}_2 \approx{}& u_1^0\cos\theta\left(\frac{2}{1+\lambda}x_{21}^a+\lambda^2\gamma x_{22}^a\right)\boldsymbol{e}_r + u_1^0\sin\theta\left(\frac{2}{1+\lambda}6_{21}^a+\lambda^2\gamma y_{22}^a\right)\boldsymbol{e}_\theta\\
&+\frac{F_t}{6\pi\mu a_1}\left(-\frac{2}{1+\lambda}y_{21}^a+\frac{1}{\lambda}y_{22}^a+\frac{6}{(1+\lambda)^2}y_{12}^b+\frac{3}{2\lambda}y_{22}^b\right)\boldsymbol{e}_\theta\\
&+\frac{\beta_1 F_n}{6\pi\mu a_1\lambda}\left(-\frac{2}{1+\lambda}y_{21}^a+\frac{1}{\lambda}y_{22}^a+\frac{6}{(1+\lambda)}y_{12}^b\right)\boldsymbol{e}_\theta, \qquad (2.26)\\
\boldsymbol{\omega}_1 \approx{}& \frac{u_1^0\sin\theta}{a_1}\left(\tfrac{3}{2}y_{11}^b+y_{12}^b\frac{6\lambda^3\gamma}{(1+\lambda)^2}\right)\boldsymbol{e}_\phi\\
&+\frac{F_t}{6\pi\mu a_1^2}\left(-\tfrac{3}{2}y_{11}^b+\frac{6}{(1+\lambda)^2}y_{12}^b+\tfrac{3}{4}y_{11}^c+\frac{6\lambda}{(1+\lambda)^3}y_{12}^c\right)\boldsymbol{e}_\phi\\
&+\frac{\beta_1 F_n}{6\pi\mu a_1^2\lambda}\left(-\tfrac{3}{2}y_{11}^b+\frac{6}{(1+\lambda)^2}y_{12}^b+\tfrac{3}{4}(1+\lambda)y_{11}^c\right)\boldsymbol{e}_\phi, \qquad (2.27)\\
\boldsymbol{\omega}_2 \approx{}& \frac{u_1^0\sin\theta}{a_1}\left(\frac{6}{(1+\lambda)^2}y_{21}^b+\tfrac{3}{2}\lambda\gamma y_{22}^b\right)\boldsymbol{e}_\phi\\
&+\frac{F_t}{6\pi\mu a_1^2}\left(-\frac{6}{(1+\lambda)^2}y_{21}^b+\frac{3}{2\lambda^2}y_{22}^b+\frac{6}{(1+\lambda)^3}y_{21}^c+\frac{3}{4\lambda^2}6_{22}^c\right)\boldsymbol{e}_\phi\\
&+\frac{\beta_1 F_n}{6\pi\mu a_1^2\lambda}\left(-\frac{6}{(1+\lambda)^2}y_{21}^b+\frac{3}{2\lambda^2}y_{22}^b+\frac{6}{(1+\lambda)^2}y_{21}^c\right)\boldsymbol{e}_\phi. \qquad (2.28)
\end{aligned}$$

In deriving (2.25) and (2.26), the identity $x_{11}^a = 2x_{12}^a/(1+\lambda) = 2x_{21}^a/(1+\lambda) = x_{22}^a/\lambda$ for two touching spheres (Jeffrey & Onishi 1984), correct to $O(\xi)$, was invoked. The rate of rotation of the line centres is determined from the relative velocity normal to the line of centres:

$$\begin{aligned}
\omega = \frac{(\boldsymbol{u}_1-\boldsymbol{u}_2)\cdot\boldsymbol{e}_\theta}{r} \approx{}& \frac{u_1^0\sin\theta}{a_1(1+\lambda)}\left(y_{11}^a-\frac{2}{(1+\lambda)}(1-\lambda^3\gamma)y_{12}^a-\lambda^2\gamma y_{22}^a\right)\\
&+\frac{F_t}{6\pi\mu a_1^2(1+\lambda)}\left[-y_{11}^a+\frac{4}{(1+\lambda)}y_{12}^a+\tfrac{3}{2}y_{11}^b+\frac{6\lambda}{(1+\lambda)^2}y_{21}^b-\frac{1}{\lambda}y_{22}^a-\frac{6}{(1+\lambda)^2}y_{12}^b-\frac{3}{2\lambda}y_{22}^b\right]\\
&+\frac{\beta_1 F_n}{6\pi\mu a_1^2\lambda(1+\lambda)}\left(-y_{11}^a+\frac{4}{(1+\lambda)}y_{12}^a+\tfrac{3}{2}(1+\lambda)y_{11}^b-\frac{1}{\lambda}y_{22}^a-\frac{6}{(1+\lambda)}y_{12}^b\right). \qquad (2.29)
\end{aligned}$$

The components of the contact force in (2.25)–(2.29) may be found by first noting from geometric considerations that

$$\cos\beta_1 = \frac{a_1+\delta+\Delta}{a_1+\delta_L} \quad\text{and}\quad \cos\beta_2 = \frac{a_2-\Delta}{a_2}, \quad\text{or}\quad \beta_1 \approx [\lambda(\xi_L-\xi)]^{1/2}, \qquad (2.30)$$

by expanding the terms and using $\beta_2 = \beta_1/\lambda$, $\beta_1 \ll 1$, $\delta/a_1 \ll 1$, $\Delta/a_2 \ll 1$ and $\delta_L/a_1 \ll 1$, where $\xi_L = 2\delta_L/(a_1 + a_2)$, as long as the two spheres remain in contact via the large bump. Here, Δ is the small distance from the edge of sphere 2 to the line passing through the contact point and normal to the line of centres When $\mathrm{d}\beta_1/\mathrm{d}t < 0$ and $\beta_1 > 0$, the separation δ increases with decreasing β_1 as the interaction proceeds and the heavy sphere 'pole vaults' upward from the surface of the light sphere using the large bump as the pole. When $\beta_1 = 0$, the maximum separation of $\delta = \delta_L$ between the nominal surfaces is reached, and then δ decreases with decreasing $\beta_1 < 0$ as the heavy sphere descends back toward the light sphere due to gravity. The component of this relative motion along the line of centres gives rise to a lubrication force that, when combined with the component of the contact force acting along the line of centres, plays the same role as the force for non-touching spheres and balances the remainder of the drag force and the net gravitational force on each of the two spheres. Hence, using (2.18) and (2.19),

$$\frac{-6\pi\mu a^2}{\delta}\frac{\mathrm{d}\delta}{\mathrm{d}t} + F_n\cos\beta_2 - F_t\sin\beta_2 = \frac{12\pi\mu a_1 u_1^0\lambda^2(1-\lambda^2\gamma)L_1\cos\theta}{(1+\lambda)^3}. \tag{2.31}$$

From (2.30) and (2.1),

$$\frac{\mathrm{d}\delta}{\mathrm{d}t} = -(a_1+\delta_L)\sin\beta_1\frac{\mathrm{d}\beta_1}{\mathrm{d}t} - a_2\sin\beta_2\frac{\mathrm{d}\beta_2}{\mathrm{d}t} \approx -a_1\beta_1(1+1/\lambda)(\omega_1-\omega),$$

and so (2.31) becomes

$$F_n - \beta_1 F_t/\lambda = \frac{12\pi\mu a_1 u_1^0\lambda^2(1-\lambda^2\gamma)L_1\cos\theta}{(1+\lambda)^3} - \frac{6\pi\mu a_1^3\lambda\beta_1(\omega_1-\omega)}{(1+\lambda)\delta}. \tag{2.32}$$

Equation (2.32) provides one relationship involving the unknown components of the contact force, F_n and F_t. When the friction force is sufficiently large to prevent slipping, then a second relationship follows from the requirement that the surface velocities of the two spheres must be equal at the point of contact:

$$\boldsymbol{u}_1 + (a_1+\delta_L)\boldsymbol{\omega}_1\times(\cos\beta_1\boldsymbol{e}_r - \sin\beta_1\boldsymbol{e}_\theta) = \boldsymbol{u}_2 - a_2\boldsymbol{\omega}_2\times(\cos\beta_2\boldsymbol{e}_r + \sin\beta_2\boldsymbol{e}_\theta). \tag{2.33}$$

Taking the dot product of this constraint with $\boldsymbol{e}_\theta$ and employing (2.18) and the limit $\delta_L \ll \min(a_1, a_2)$ yields

$$(a_1+a_2)\omega \approx a_1\omega_1 + a_2\omega_2. \tag{2.34}$$

Substituting (2.27)–(2.29) into (2.32) and (2.34), and eliminating small terms of $O(\beta_1^2) = O(\xi_L - \xi)$, allows determination of the individual components of the contact force:

$$\frac{F_t}{6\pi\mu a_1 u_1^0} \approx \frac{\left((1+\lambda)^3\alpha_1 + 2\beta_1^2(1+\lambda)(\alpha_1\alpha_8+\alpha_5\alpha_6)/\xi\right)\sin\theta - 2\beta_1\alpha_5\lambda(1-\lambda^2\gamma)L_1\cos\theta}{(1+\lambda)^3\alpha_2 + (1+\lambda)^3\beta_1^2\alpha_5/\lambda^2 + 2\beta_1^2(1+\lambda)(\alpha_2\alpha_8+\alpha_5\alpha_7)/\xi}, \tag{2.35}$$

$$\frac{F_n}{6\pi\mu a_1 u_1^0} \approx \frac{2\left((1-\lambda^2\gamma)\lambda^2 L_1\cos\theta - \beta_1^2(1+\lambda)\dfrac{\alpha_6}{\xi}\right)\sin\theta + \beta_1\left(2(1+\lambda)\dfrac{\alpha_7}{\xi} + \dfrac{(1+\lambda)^3}{\lambda}\right)\dfrac{F_t}{(6\pi\mu a_1 u_1^0)}}{(1+\lambda)^3 + 2\beta_1^2(1+\lambda)\alpha_6/\xi}, \tag{2.36}$$

where

$$\alpha_1 = (1+\lambda)k_7 - k_1 - \lambda k_4, \quad \alpha_2 = k_2 + \lambda k_5 - (1+\lambda)k_8, \quad \alpha_3 = k_6 - k_4, \quad (2.37a, b, c)$$

$$\alpha_4 = k_2 - k_5, \quad \alpha_5 = k_3 + \lambda k_6 - (1+\lambda)k_9, \quad \alpha_6 = k_1 - k_7, \quad (2.37d, e, f)$$

$$\alpha_7 = k_8 - k_2, \quad \alpha_8 = k_3 - k_9, \quad \alpha_9 = k_4 - k_1, \quad (2.37g, h, i)$$

and

$$k_1 = \tfrac{3}{2}y_{11}^b + y_{12}^b \frac{6\lambda^3\gamma}{(1+\lambda)^2}, \quad (2.38a)$$

$$k_2 = -\tfrac{3}{2}y_{11}^b + \frac{6}{(1+\lambda)^2}y_{12}^b + \tfrac{3}{4}y_{11}^c + \frac{6\lambda}{(1+\lambda)^3}y_{12}^c, \quad (2.38b)$$

$$k_3 = -\tfrac{3}{2}y_{11}^b + \frac{6}{(1+\lambda)^2}y_{12}^b + \tfrac{3}{2}(1+\lambda)y_{11}^c, \quad (2.38c)$$

$$k_4 = \frac{6}{(1+\lambda)^2}y_{21}^b + \tfrac{3}{2}\lambda\gamma y_{22}^b, \quad (2.38d)$$

$$k_5 = -\frac{6}{(1+\lambda)^2}y_{21}^b + \frac{3}{2\lambda^2}y_{22}^b + \frac{6}{(1+\lambda)^3}y_{21}^c + \frac{3}{4\lambda^2}y_{22}^c, \quad (2.38e)$$

$$k_6 = -\frac{6}{(1+\lambda)^2}y_{21}^b + \frac{3}{2\lambda^2}y_{22}^b + \frac{6}{(1+\lambda)}y_{21}^c, \quad (2.38f)$$

$$k_7 = \frac{1}{1+\lambda}\left[y_{11}^a - \frac{2}{(1+\lambda)}(1-\lambda^3\gamma)y_{12}^a - \lambda^2\gamma y_{22}^a\right], \quad (2.38g)$$

$$k_8 = \frac{1}{1+\lambda}\left[-y_{11}^a + \frac{4}{(1+\lambda)}y_{12}^a + \tfrac{3}{2}y_{11}^b + \frac{6\lambda}{(1+\lambda)^2}y_{21}^a - \frac{1}{\lambda}y_{22}^a - \frac{6}{(1+\lambda)^2}y_{12}^b - \frac{3}{2\lambda}y_{22}^b\right], \quad (2.38h)$$

$$k_9 = \frac{1}{1+\lambda}\left[-y_{11}^a + \frac{4}{(1+\lambda)}y_{12}^a + \tfrac{3}{2}(1+\lambda)y_{11}^b - \frac{1}{\lambda}y_{22}^a - \frac{6}{(1+\lambda)}6_{12}^b\right]. \quad (2.38i)$$

All of the above functions are evaluated at the dimensionless centre-to-centre separation $s = 1 + \xi$.

Rolling without slipping is limited to small angles $\theta \leqslant \theta_s$, so that the friction force F_t does not exceed its maxmum value of $\mu_f F_n$, where μ_f is the coefficient of rolling friction. Typical values for μ_f are in the range 0.05–0.4 (Galvin *et al.* 2001). From (2.35) and (2.36), the angle at which slipping first occurs is

$$\theta_s \approx \tan^{-1}\left(\frac{c_1 + \mu_f c_2}{c_3 + \mu_f c_4}\right), \quad (2.39)$$

where

$$c_1 = 2\beta_1\alpha_5\lambda(1-\lambda^2\gamma)L_1\big((1+\lambda)^3 + 2\beta_1^2(1+\lambda)\alpha_8/\xi\big), \quad (2.40a)$$

$$c_2 = 2(1-\lambda^2\gamma)L_1\gamma\big(\lambda(1+\lambda)^3\alpha_2 + (1+\lambda)^3\alpha_5\beta_1^2/\lambda^2 + 2(1+\lambda)\beta_1^2(\alpha_2\alpha_8 + \alpha_5\alpha_7)/\xi - \beta_1^2\alpha_5(2\lambda(1+\lambda)\alpha_7/\xi + (1+\lambda)^3/\lambda)\big), \quad (2.40b)$$

$$c_3 = \big((1+\lambda)^3 + 2\beta_1^2(1+\lambda)\alpha_8/\xi\big)\big((1+\lambda)^3\alpha_1 + 2(1+\lambda)\beta_1^2(\alpha_1\alpha_8 + \alpha_5\alpha_6)/\xi\big), \quad (2.40c)$$

$$c_4 = (2\beta_1\lambda(1+\lambda)\alpha_6/\xi)\big((1+\lambda)^3\alpha_2 + (1+\lambda)^3\alpha_5\beta_1^2/\lambda^2 + 2(1+\lambda)\beta_1^2(\alpha_2\alpha_8 + \alpha_5\alpha_7)/\xi\big) - \beta_1\big((1+\lambda)^3\alpha_1 + 2(1+\lambda)\beta_1^2(\alpha_1\alpha_8 + \alpha_5\alpha_6)/\xi\big)(2\lambda(1+\lambda)\alpha_7/\xi + (1+\lambda)^3/\lambda). \quad (2.40d)$$

For $\theta > \theta_s$, slipping in addition to rolling occurs. Then, (2.34) no longer holds. Instead, from (2.32),

$$\frac{F_t}{6\pi\mu a_1 u_1^0} = \frac{\mu_f F_n}{6\pi\mu a_1 u_1^0} \approx \frac{\mu_f(2(1-\lambda^2\gamma)\lambda^2 L_1\cos\theta - 2\beta_1\lambda(1+\lambda)\alpha_6\sin\theta/\xi)}{(1+\lambda)^3(1-\beta_1\mu_f/\lambda) - 2\beta_1\lambda(1+\lambda)(\mu_f\alpha_7 - \beta_1\alpha_8/\lambda)/\xi}, \quad (2.41)$$

where μ_f is now the coefficient of sliding friction. Finally, loss of contact with the large bump occurs when F_n given by (2.41) with slipping, or (2.34) without slipping, is no longer positive.

2.3. *Contact with small bumps*

Geometrical constraints require that

$$\Phi_L = \Phi_{L,\min} \approx \sqrt{\frac{2(\delta_L^A - \delta_S)}{a_1(1+1/\lambda)}} + \sqrt{\frac{2(\delta_L^B - \delta_S)}{a_1(1+1/\lambda)}}, \quad (2.42)$$

for the spheres to simultaneously make contact on the small bumps and two adjacent large bumps, where Φ_L is the angle between two successive large bumps along the equator of sphere 1 and the heights of the two large bumps are δ_L^A and δ_L^B. If Φ_L is smaller than that given by (2.42), then the two spheres are not able to contact via the small bumps. For the special case where the two large bumps are identical ($\delta_L^A = \delta_L^B = \delta_L$), contact with the small bumps can occur only if

$$\Phi_L \geqslant \Phi_{L,\min} \approx 2\sqrt{\lambda(\xi_L - \xi_S)}. \quad (2.43)$$

When the above constraint is satisfied, and the separation between the nominal surfaces decreases to $\delta = \delta_S$, then the two spheres make contact via the small bumps and the normal component of the contact force is directed along the line of centres. This case was analysed by Davis (1992) and Zhao & Davis (2002), except that the previous work was restricted to when the light sphere is neutrally buoyant. The modified equations for the present case follow directly from those in the previous subsection, but with $\beta_1 = \beta_2 = 0$ and $\xi = \xi_S = 2\delta_S/(a_1 + a_2)$.

2.4. *Simultaneous contact with the small bumps and a large bump*

In the work of Galvin *et al.* (2001) for a sphere moving down an inclined plane, a special case occurs when the angle of inclination of the plane from horizontal is small enough that the sphere is not able to rotate over a large bump. A similar situation may occur for two spheres in contact at small angle θ. Suppose two spheres in contact with small bumps and rotating with $\mathrm{d}\beta_1/\mathrm{d}t < 0$ encounter a large bump. If $\omega_1 > \omega$, as calculated from (2.27) and (2.29) with F_n and F_t from (2.35) and (2.36) for no slipping or (2.41) for slipping, then (2.1) indicates that the spheres are not able to ascend the second large bump and so do not lose contact with the small bumps. Therefore, the two spheres will contact each other simultaneously with the small bumps and the large bump. To remain in this condition, the two spheres must move in rigid-body motion ($\omega = \omega_1 = \omega_2$), or the heavy sphere must slide along the light sphere without pivoting ($\omega = \omega_1 \neq \omega_2$). The forces and torques acting on the two spheres must be modified from (2.21–2.24) to include contact forces from both the large and small bumps:

$$\boldsymbol{F}_1 = \left(F_1^g\cos\theta - F_n^L\cos\beta_2 + F_t^L\sin\beta_2 - F_n^S\right)\boldsymbol{e}_r + \left(F_1^g\sin\theta - F_n^L\sin\beta_2 - F_t^L\cos\beta_2 - F_t^S\right)\boldsymbol{e}_\theta, \quad (2.44)$$

$$\boldsymbol{F}_2 = \left(F_2^g \cos\theta + F_n^L \cos\beta_2 - F_t^L \sin\beta_2 + F_n^S\right)\boldsymbol{e}_r + \left(F_2^g \sin\theta + F_n^L \sin\beta_2 + F_t^L \cos\beta_2 + F_t^S\right)\boldsymbol{e}_\theta, \quad (2.45)$$

$$\boldsymbol{L}_1 = (a_1 + \delta_L)\left(F_n^L \sin(\beta_1 + \beta_2) + F_t^L \cos(\beta_1 + \beta_2)\right)\boldsymbol{e}_\phi + (a_1 + \delta_S)F_t^S \boldsymbol{e}_\phi, \quad (2.46)$$

$$\boldsymbol{L}_2 = a_2\left(F_t^L + F_t^S\right)\boldsymbol{e}_\phi, \quad (2.47)$$

where the superscripts L and S refer to contact on the large and small bumps, respectively.

The translational and rotational velocities of the two spheres can be found through (2.25)–(2.29), but using $F_t^L \cos\beta_2 + F_t^S \approx F_t^L + F_t^S$ in place of F_t, and F_n^L in place of F_n (F_n^S does not affect the translational and rotational velocities, since this force component is along the line of centres). Because $\delta = \delta_S$ is constant, the force balance along the line of centres from (2.31) yields

$$F_n^L + F_n^S - \beta_1 F_t^L/\lambda \approx \frac{12\pi\mu a_1 u_1^0 \lambda^2(1-\lambda^2\gamma)L_1\cos\theta}{(1+\lambda)^3}. \quad (2.48)$$

Equations (2.33)–(2.34) still hold for small angles when friction is sufficiently large to prevent slipping. In this case, substituting (2.25)–(2.29) into the relations $\omega = \omega_1 = \omega_2$, and eliminating small terms of $O(\beta_1^2) = O(\xi_L - \xi)$, allows the determination of the relevent components of the contact force:

$$\frac{F_n^L}{6\pi\mu a_1 u_1^0} \approx \frac{\lambda}{\beta_1}\frac{(\alpha_4\alpha_6 - \alpha_9\alpha_7)\sin\theta}{(\alpha_3\alpha_7 - \alpha_4\alpha_8)}, \quad (2.49)$$

$$\frac{F_t^L + F_t^S}{6\pi\mu a_1 u_1^0} \approx \frac{\dfrac{\beta_1}{\lambda}\dfrac{F_n^L}{6\pi\mu a_1 u_1^0}\alpha_3 + \alpha_9\sin\theta}{\alpha_4} = \frac{(\alpha_3\alpha_6 - \alpha_9\alpha_8)\sin\theta}{(\alpha_3\alpha_7 - \alpha_4\alpha_8)}. \quad (2.50)$$

The solid-body rotation without slipping ends when the θ reaches the critical angle θ_s, with the combined friction force $F_t^L + F_t^S$ equal to $\mu_f(F_n^L + F_n^S)$. From (2.48) and (2.50), the angle at which slipping first occurs is

$$\theta_s \approx \tan^{-1}\left\{\left[\frac{2\lambda^2(1-\lambda^2\gamma)L_1\mu_f}{(1+\lambda)^3}\right]\Bigg/\left[\left(\frac{\alpha_3\alpha_6 - \alpha_9\alpha_8}{\alpha_3\alpha_7 - \alpha_4\alpha_8}\right)\left(\frac{\alpha_8 - \alpha_7\mu_f^2}{\alpha_8\mu_f}\right) + \frac{\alpha_6}{\alpha_8}\mu_f\right]\right\}. \quad (2.51)$$

During slipping, $\omega = \omega_1 \neq \omega_2$, and the relevant components of the contact forces are

$$\frac{F_t^L + F_t^S}{6\pi\mu a_1 u_1^0} \approx \left[\frac{2\lambda^2(1-\lambda^2\gamma)L_1\cos\theta}{(1+\lambda)^3} - \frac{\alpha_6}{\alpha_8}\mu_f\sin\theta\right]\Bigg/\left(\alpha_8 - \alpha_7\mu_f^2\right), \quad (2.52)$$

$$\frac{F_n^L}{6\pi\mu a_1 u_1^0} \approx \frac{\lambda}{\beta_1}\frac{\alpha_7\left(F_t^L + F_t^S\right) - \alpha_6\sin\theta}{\alpha_8}. \quad (2.53)$$

Finally, loss of contact with the small bumps occurs when F_n^S calculated from (2.48) and (2.49) or (2.53) is no longer positive as θ increases beyond a certain value. Then, since the contact is not able to impart a tensile force, the nominal separation increases from δ_S as the heavy sphere 'pole vaults' away from the light sphere using the large bump as a pivot.

2.5. *Simultaneous contact with two large bumps*

If the constraint given by (2.42) or (2.43) is not met, then the two spheres may make simultaneous contact via two large bumps. This case will occur when a second large

bump is encountered before contact is lost with the first large bump. For simultaneous contact with two large bumps to continue, $\mathrm{d}\beta_1/\mathrm{d}t = 0$, and the spheres are not able to ascend the second large bump. Instead, they stay together and rotate like a rigid body ($\omega = \omega_1 = \omega_2$) or slide along each other ($\omega = \omega_1 \neq \omega_2$). Following a similar analysis as in § 2.4, the forces and torques on the two spheres are

$$\boldsymbol{F}_1 = \big(F_1^g \cos\theta - F_n^A \cos\beta_2 - F_n^B \cos\beta_2 + F_t^A \sin\beta_2 - F_t^B \sin\beta_2\big)\boldsymbol{e}_r + \big(F_1^g \sin\theta - F_n^A \sin\beta_2 + F_n^B \sin\beta_2 - F_t^A \cos\beta_2 - F_t^B \cos\beta_2\big)\boldsymbol{e}_\theta, \quad (2.54)$$

$$\boldsymbol{F}_2 = \big(F_2^g \cos\theta + F_n^A \cos\beta_2 + F_n^B \cos\beta_2 - F_t^A \sin\beta_2 + F_t^B \sin\beta_2\big)\boldsymbol{e}_r + \big(F_2^g \sin\theta + F_n^A \sin\beta_2 - F_n^B \sin\beta_2 + F_t^A \cos\beta_2 + F_t^B \cos\beta_2\big)\boldsymbol{e}_\theta, \quad (2.55)$$

$$\boldsymbol{L}_1 = (a_1 + \delta_L)\big(F_n^A \sin(\beta_1 + \beta_2) - F_n^B \sin(\beta_1 + \beta_2) + F_t^A \cos(\beta_1 + \beta_2) + F_t^B \cos(\beta_1 + \beta_2)\big)\boldsymbol{e}_\phi, \quad (2.56)$$

$$\boldsymbol{L}_2 = a_2\big(F_t^A + F_t^B\big)\boldsymbol{e}_\phi, \quad (2.57)$$

where the superscripts A and B refer to the two large bumps, which are located at angles $\beta_1 = \Phi_L/2$ and $-\Phi_L/2$, respectively, along the equator of sphere 1 from the line of centres. For simplicity, we assume here that the two large bumps are of equal height. From (2.2)–(2.5) and (2.54)–(2.57), it is seen that the resulting motion for simultaneous contact via two large bumps is the same as that for simultaneous contact via the small bumps and the large bump, except that $F_n^A + F_n^B$ replaces $F_n^L + F_n^S$ in (2.48), $F_n^A - F_n^B$ replaces F_n^L in (2.49) and (2.53), and $F_t^A + F_t^B$ replaces $F_t^L + F_t^S$ in (2.50) and (2.51).

The simultaneous contact with two large bumps ends when the contact force via the first large bump is zero or, equivalently, if the analysis of § 2.2 gives rise to $\mathrm{d}\beta_1/\mathrm{d}t = \omega_1 - \omega < 0$ for contact with the second large bump only. Then, the spheres will lose contact with the first large bump and be able to asecnd the second large bump.

3. Experimental materials and methods

The experiments were carried out at room temperature (22 °C–25 °C) in a vessel made of Plexiglas, and filled with a Newtonian fluid consisting of 97.4% polyalkylene glycol and 2.6% tetrabromoethane by weight. From Zhao & Davis (2002), the kinematic viscosity of the fluid is $\nu = 363\,\mathrm{cm^2\,s^{-1}}$ at 22 °C and $\nu = 308\,\mathrm{cm^2\,s^{-1}}$ at 25 °C. The fluid density is $\rho = 1.112\,\mathrm{g\,cm^{-3}}$ at 22 °C and $\rho = 1.111\,\mathrm{g\,cm^{-3}}$ at 25 °C. The vessel was fixed on a two-dimensional stand and could be rotated about a horizontal axis. A teflon sphere ($\rho_1 = 2.154\,\mathrm{g\,cm^{-3}}$, $a_1 = 0.318\,\mathrm{cm}$) was used as the heavy sphere, and a nylon sphere ($\rho_2 = 1.134\,\mathrm{g\,cm^{-3}}$, $a_2 = 0.318\,\mathrm{cm}$) was used as the light sphere. Two distinct roughness sizes were created by using the natural roughness for the small bumps and then adding artificial roughness to the heavy sphere for the large bumps. Covered with a thin layer of instant glue, the teflon sphere was rolled on a sand glass on which a few glass beads with diameter of about 0.1 mm were sparsely distributed. The glass beads stuck to the surface of the teflon sphere and created the large surface roughness elements (figure 2). As described by Smart & Leighton (1989), the hydrodynamic roughness of a sphere can be measured by allowing it to settle onto a smooth plane in a viscous fluid and then inverting the plane and measuring the

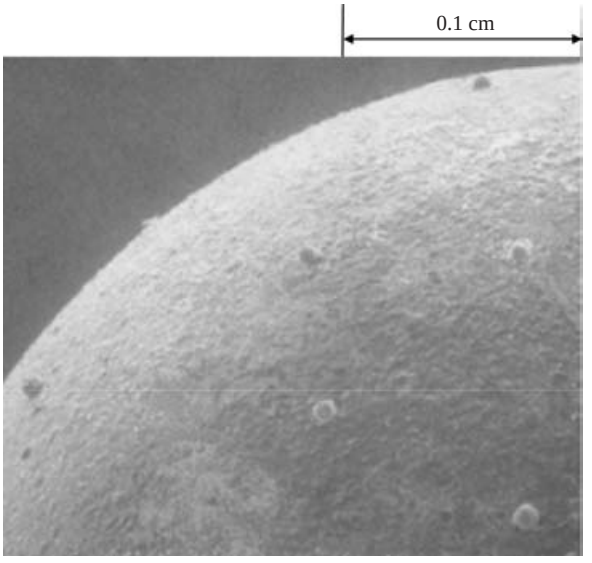

FIGURE 2. Scanning electron micrograph of artificially roughened teflon sphere with small glass beads on its surface.

times t_a and t_d for it to fall one radius and one diameter, respectively, from the plane. The initial separation between the nominal surfaces of the sphere and plane is then determined using

$$\delta/a = 2\exp\left(2 - \frac{t_d}{(t_d - t_a)}(1 + \ln 2)\right). \tag{3.1}$$

Using this method, the natural roughness size of the nylon sphere was measured at 8 μm, and that of the teflon sphere (with a thin layer of dried glue) was measured at 10 μm. To verify the size of the large roughness elements on the teflon sphere, the method of Galvin *et al.* (2001) was used. The teflon sphere was allowed to move due to gravity in a viscous fluid down a smooth plane inclined only a few degrees from vertical. The plane was then inverted to horizontal (facing down), and (3.1) was used to find the large bump size, which was 95 μm. Finally, scanning electron micrographs (e.g. figure 2) yield an average value for the angle between two adjacent large bumps of $\Phi_L = 29°$.

For the two-sphere interaction experiments, the two spheres were sequentially introduced into the vessel. Two digital camcorders (Canon ELURA) were used to observe and record the motion of the spheres from both the top and side of the vessel (figure 3), and image analysis was performed as described by Zhao & Davis (2002). Translational and rotational motions of the spheres with natural roughness only were reported in our previous work (Zhao & Davis 2002), showing considerable scatter in the data, but with at least qualitative agreement with the theory and verifying the roll/slip model for the contact interaction with a single bump size. In the present work, the focus of the experiments is on how the nominal separation between the two spheres changes after contact is made when there are multiple roughness scales.

After the spheres were allowed to contact each other and rotate to a specified angle θ, the whole system was rotated about a horizontal axis to a position so that the line of centres was vertical (with the heavy sphere directly below the light one). The heavy sphere then fell away from contact with the light sphere. By integrating (2.31), the

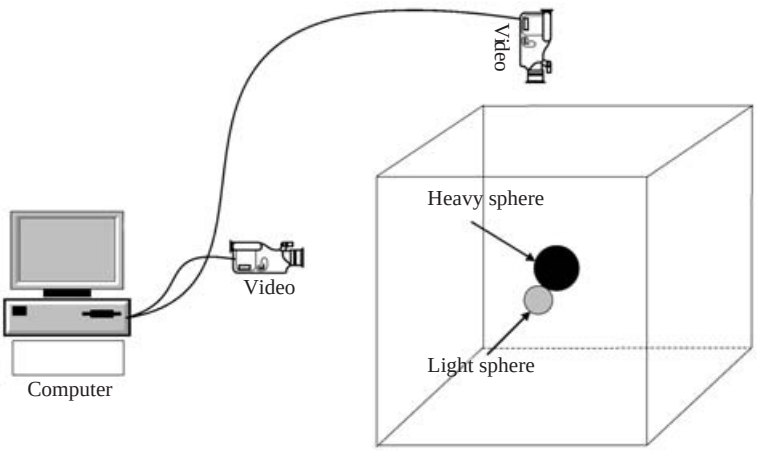

FIGURE 3. Schematic of the experimental setup.

dimensionless nominal separation between the two spheres at the time when system was inverted is

$$\xi_0 = \frac{t_1 \ln \xi_2 - t_2 \ln \xi_1}{t_1 - t_2}, \tag{3.2}$$

where t_1 and t_2 are the times for the dimensionless nominal separation to increase from ξ_0 to ξ_1 and ξ_2, respectively. The values of ξ_1 and ξ_2 were selected to be much less than unity (e.g. $\xi \approx 0.05$ and $\xi_2 \approx 0.10$), so that (2.31) is accurate. The experiments were repeated many times, allowing the distributions of apparent hydrodynamic roughness to be found for several values of θ.

4. Model results and discussion

4.1. *Different stages of contact*

The theory described in § 2 was used to analyse the different contact stages which two spherical particles with microscopic surface roughness experience during sedimentation in viscous fluid. To reduce the number of parameters, we restrict our attention to equal-size spheres where the lighter one is nearly neutrally buoyant sphere (as also done in the experiments), and to large roughness elements of single size and spacing.

Figure 4 shows the dimensionless hydrodynamic separation and the rotational velocities of the heavy and light spheres versus the angle between the line of centres and vertical, starting from $\theta_0 = 10^\circ$ and $\beta_0 = 0^\circ$ at $t = 0$, with $\xi_L = 0.06$, $\xi_S = 0.012$, $\Phi_L = 45^\circ$, $\gamma = 0.02$, $\lambda = 1$, and $\mu_f = 0.15$ (Galvin *et al.* 2001). For comparison with the roll/slip model with only one bump size, $\xi = 0.012$ was used as the dimensionless single bump height. Arrows are used to represent the transitions between the different contact stages, and figure 5 illustrates the relative positions of the two spheres at these transitions.

At the initial contact (IC) point ($\theta = 10^\circ$, $\beta_1 = 0^\circ$ and $\xi = 0.06$), the two spheres are assumed to contact each other at the apex of a large bump. Under the action of both hydrodynamic and contact forces, the spheres subsequently descend from the large bump by rotating clockwise with $\omega_2 > \omega > \omega_1 > 0$. Hence, $\mathrm{d}\beta_1/\mathrm{d}t = \omega_1 - \omega < 0$, and

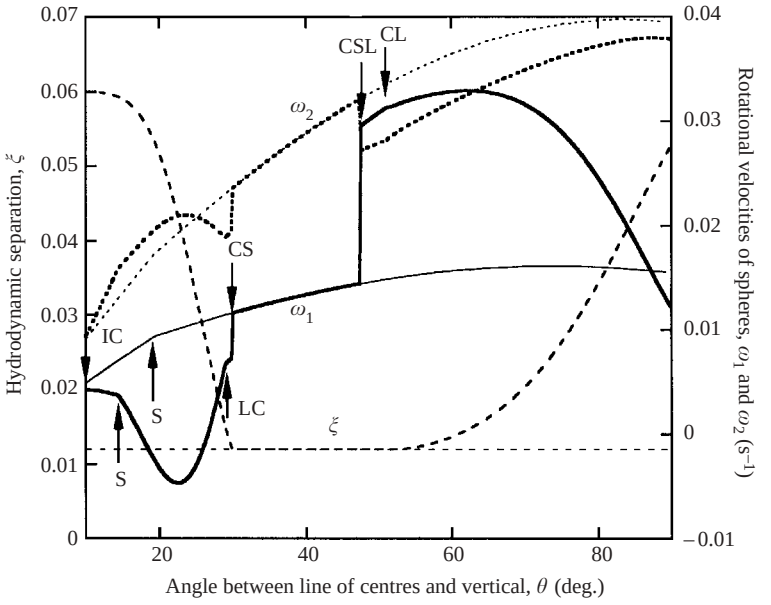

FIGURE 4. The dimensionless hydrodynamic separation (dashed line) and the rotational velocities of the heavy (solid line) and light (dotted line) spheres versus the angle between the line of centres and vertical for the roll/slip model for one bump height (thin lines) and the current model for two bump heights (thick lines), starting from initial conditions of $\theta = 10°$, $\beta_1 = 0°$ at $t = 0$, with $\xi_L = 0.06$, $\xi_S = 0.012$, $\mu_f = 0.15$, $\Phi_L = 45°$, $\gamma = 0.02$ and $\lambda = 1$; for the thin lines, $\xi = 0.012$ was used as the dimensionless bump height. S indicates where slipping begins. See the caption of figure 5 for definitions of the other transition labels. The rotational velocities may be made dimensionless by dividing by $u_1^0/a_1 = 0.2\,s^{-1}$ for the conditions of the experiments.

so the rotation of the heavy sphere about the contact point is counterclockwise. As the heavy sphere descends from the apex of the large bump, however, a lubrication force develops and reduces the normal component of the contact force and, hence, the maximum value of the friction force is also reduced, which causes the rotational velocities of heavy and light spheres to decrease and increase, respectively. At the slipping (S) position ($\theta = 14.6°$, $\beta_1 = -2.3°$ and $\xi = 0.059$), the friction force between the spheres reaches its maximum value. After that, the spheres exhibit a combination of rolling and slipping, and the rotational velocity of the heavy sphere decreases further to a minimum value and then increases again, whereas the rotational velocity of the light sphere increases to a maximum value and then decreases. Indeed, for $17.6° < \theta < 26.4°$, we find $\omega_1 < 0$, indicating that the heavy sphere rotates counterclockwise about its centre for a brief period.

At the loss-of-contact (LC) point ($\theta = 29.0°$, $\beta_1 = -17.3°$ and $\xi = 0.015$), the lubrication force resisting the relative approach of the nominal surfaces of the two spheres is sufficiently strong that it balances gravity and the additional hydrodynamic forces, so that the normal component of the contact force becomes zero and the two spheres lose physical contact. During the period of no contact, the separation continues to decrease until the spheres contact the small bumps (CS, with $\theta = 30.0°$, $\beta_1 = -17.9°$ and $\xi = 0.012$). Due to the frictional contact forces introduced via the small bumps, the rotational velocities of both spheres are increased. We assume that the small bumps are of equal size and distributed with sufficient density on the

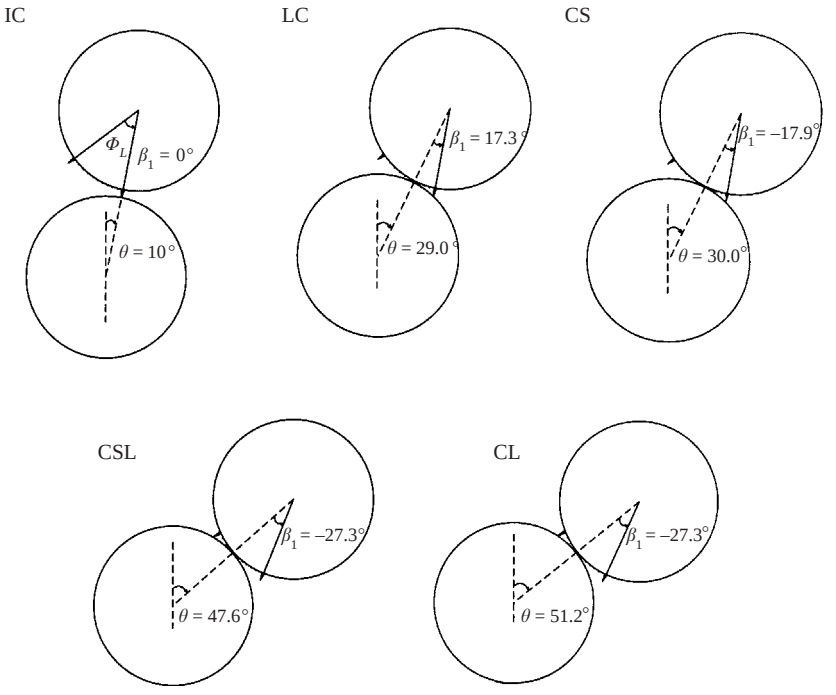

FIGURE 5. Sequential configurations for the different contact stages of two spheres with the same initial conditions and parameters as in figure 4; IC = initial contact with a large asperity, LC = loss of contact, CS = contact with small asperities, CSL = contact with small asperities and a second large asperity, CL = ascending the second large asperity with loss of contact with small asperities. Stage C2L is contact with two large asperities, which is not possible with the parameters of figure 4.

sphere surfaces to maintain $\xi = \xi_S = 0.012$. The interaction during this contact stage is then identical to that analysed previously for a single bump size (Davis 1992; Zeng *et al.* 1996; Zhao & Davis 2002). In the present case, the two spheres roll and slip around each other (the critical angle for slipping to begin is only 20°) with a constant separation ($\xi = \xi_S = 0.012$) until they encounter a second large bump.

Point CSL ($\theta = 47.6°$, $\beta_1 = 27.3°$, $\xi = 0.012$) represents the beginning of the contact with a second large lump, which we assume here to be the same size as the first large bump, with simultaneous contact with the small bumps. From figure 1, the contact forces through the second large bump favour the clockwise rotation of the heavy sphere and reduce the clockwise rotation of the light sphere, as verified in figure 4. Immediately following point CSL, the velocities of the heavy sphere and the line of centres are equal ($\omega = \omega_1$), which implies that the spheres continue to simultaneously make contact with the small bumps and the large bump. However, the rotational velocities of the heavy and light spheres are not same ($\omega = \omega_1 \neq \omega_2$), which means that the spheres in this case undergo a sliding motion rather than locking together in rigid-body motion.

With increasing angle θ, the normal component of the contact force via the second large bump decreases. At point CL ($\theta = 51.2°$, $\beta_1 = -27.3°$, $\xi = 0.012$), it reaches zero and the spheres are able to begin rising away from contact via the small bumps and ascend the second large bump. After that, the nominal separation between the two spheres increases. However, for the current parameter values, the apex ($\xi = \xi_L$) of

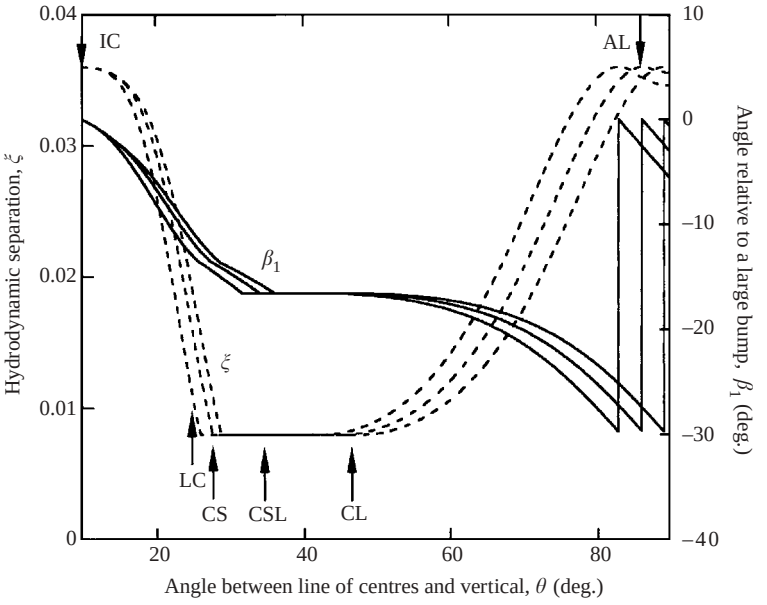

FIGURE 6. Effect of varying the friction coefficient on the dimensionless hydrodynamic separation (dashed lines) and the angle between the line of centres and the line connecting the centre of the heavy sphere and a large bump (solid lines) versus the angle between line of centres and vertical, starting from an initial condition of $\theta = 10°$ and $\beta_1 = 0°$ at $t = 0$, with $\xi_L = 0.036$, $\xi_S = 0.008$, $\Phi_L = 30°$, $\gamma = 0.02$, $\lambda = 1$ and $\mu_f = 0.10$, 0.15 and 0.20 (left to right). The arrows are for $\mu_f = 0.15$ and correspond to the stages described in the caption of figure 5, but with AL = reaching the apex of the second large bump.

the second large bump is not reached before the line of centres becomes horizontal ($\theta = 90°$) and the heavy sphere falls away from the light sphere.

Compared with the roll/slip model of Davis (1992) for a single bump size, the current model for two bump sizes predicts a much more complex contact behaviour. Besides the nominal separation varying between the small and large bump heights, the rotational velocities exhibit discontinuities when bumps of a different size are encountered. The changes in rotational velocities are most pronounced for the sphere on which the large asperities reside.

4.2. *Effects of varying parameter values*

The interaction of two spheres with multiple roughness scales is strongly affected by several parameters, including the coefficient of friction, μ_f, the bump sizes, ξ_L and ξ_S, the angle between two adjacent large bumps, Φ_L, and the initial conditions θ_0 and β_0. Figure 6 shows the dimensionless hydrodynamic separation and the angle between the line of centres and the line connecting the centre of the heavy sphere and a large bump versus the angle which the line of centres makes with the gravity vector, starting from an initial condition of $\theta_0 = 10°$ and $\beta_0 = 0°$, with $\xi_L = 0.036$, $\xi_S = 0.008$, $\Phi_L = 30°$, $\gamma = 0.02$ and $\lambda = 1$, and friction coefficients of $\mu_f = 0.10$, 0.15 and 0.20. The overall behaviour is similar to that shown in figures 4 and 5. The spheres experience five contact stages: descending from initial contact with the first large bump, loss of contact, contact with small bumps, contact simultaneously with small bumps and a second large bump, and ascending the second large bump with loss of contact with the small bumps. In this case, however, the apex of the second large bump (point AL

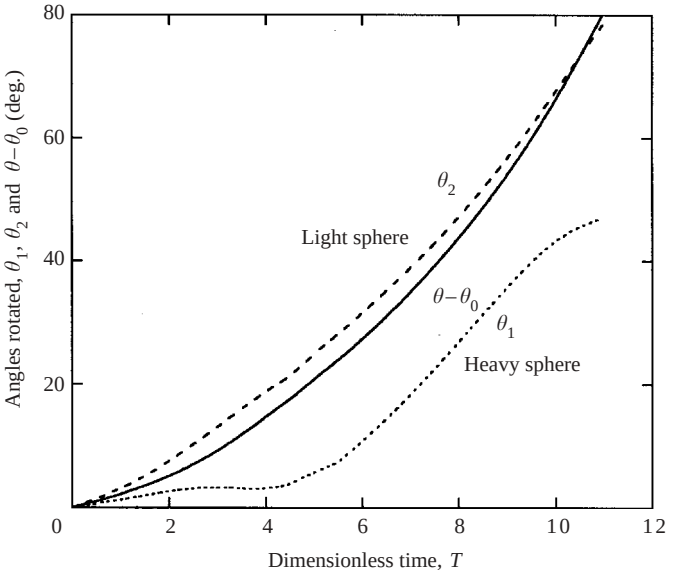

FIGURE 7. The angle through which the line of centres rotated (solid line) and the angles through which the heavy (dotted line) and light (dashed line) spheres rotated versus dimensionless time since the contact occurred for the same conditions as in figure 6 with $\mu_f = 0.15$.

in figure 6) is reached before the point where $\theta = 90°$ and the spheres separate. At point AL, β_1 is redefined to be the angle between the line of centres and the second large bump and so jumps back to 0°. Changing the coefficient of friction has only a modest influence on the results. Increasing μ_f generally leads to an increase in the angle θ for each transition point, because the normal components of gravity and the contact force must become smaller to achieve the same frictional force.

The angles through which the two spheres and their line of centres rotated as functions of time are displayed in figure 7 for the same conditions as in figure 6 and $\mu_f = 0.15$. Here, θ_i is the angle through which sphere i rotated starting at $t = 0$ when contact first occurred. The dimensionless time is defined as $T = tu_1^0/a_1$. Compared with the rotation of the light sphere and the line of centres, the heavy sphere rotated less in the beginning, which is consistent with the above analysis that, when descending from the first large bump, the normal component of the contact force opposes the clockwise rotation of the heavy sphere.

The effect of varying the large bump size is shown in figure 8. When the dimensionless large bump height is $\xi_L = 0.02$, the spheres make contact via the small bumps at a smaller θ than for $\xi_L = 0.036$ (figure 6). Also, when contact via the second large bump occurs, the rotational velocity of the heavy sphere shows a clear difference from that of the line of centres from vertical, which indicates that the spheres are able to ascend the large bump when $\xi_L = 0.02$ without remaining in contact with the small bumps, and so no stage CSL is observed in this case. When the large bump height is $\xi_L = 005$, the spheres are able to make contact with two large bumps simultaneously, as indicated by (42), and so no contact via the small bumps occurs in this case (stage CS). Stage C2L in figure 8 for $\xi_L = 0.05$ marks the beginning of simultaneous contact with two large bumps. Since the normal components of the contact forces prevent the heavy sphere from rolling over the second large bump, the spheres stick together

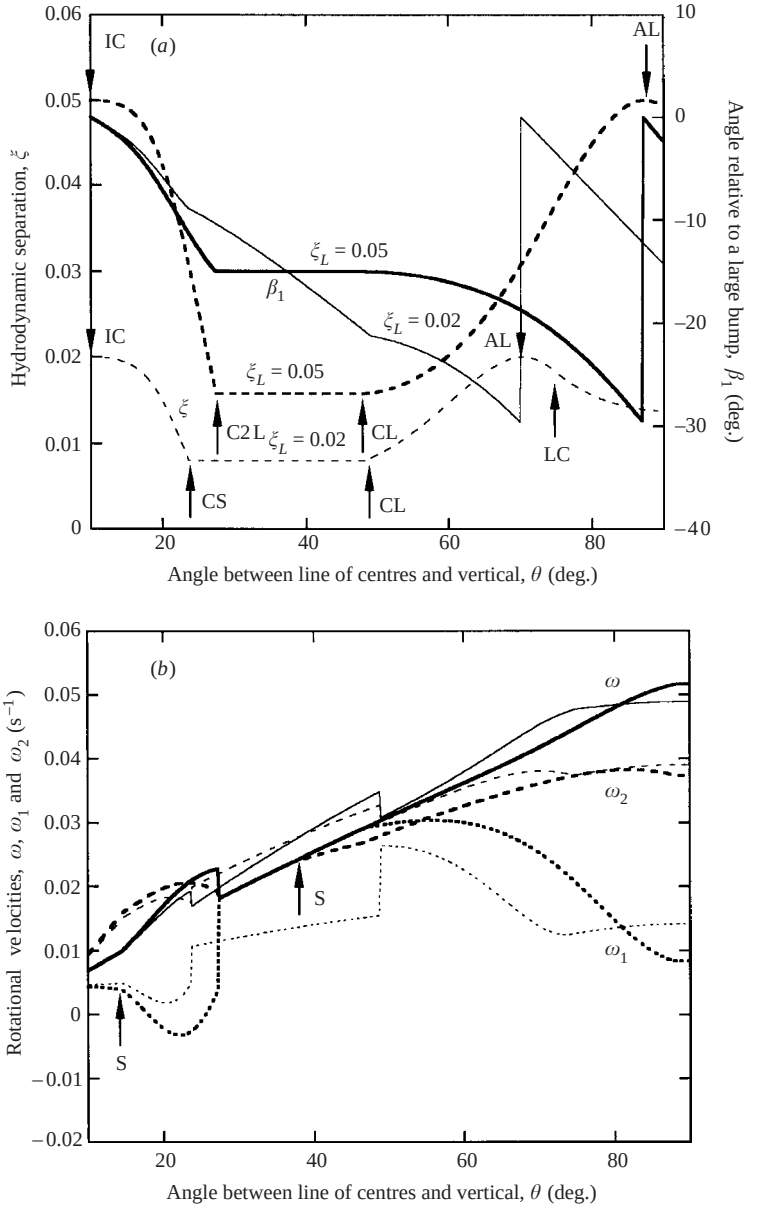

FIGURE 8. Effect of varying the large bump height on (*a*) the dimensionless hydrodynamic separation (dashed lines) and the angle between the line of centres and the line connecting the centre of the heavy sphere and a large bump (solid lines) and (*b*) the rotational velocities of the heavy (dotted lines) and light (dashed lines) sphere and the line of centres (solid lines) versus the angle between the line of centres and vertical, for the same conditions as in figure 6 except $\mu_f = 0.15$ and $\xi_L = 0.02$ (thin lines) and 0.05 (thick lines). S indicates where slipping begins. The rotational velocities may be made dimensionless by dividing by $u_1^0/a_1 = 0.2\,\mathrm{s}^{-1}$ for the conditions of the experiments.

and rotate like a rigid body ($\omega = \omega_1 = \omega_2$) until slipping begins (point S in figure 8*b*). Then, the rotational velocity of the heavy sphere coincides with that of the line of centres from vertical but not with that of the light sphere ($\omega = \omega_1 \neq \omega_2$). After that,

when θ is large enough so that the normal components of gravity and the contact forces are sufficiently reduced, the spheres begin to ascend the second large bump (stage CL) and the rotational velocity of the heavy sphere differs from that of the line of centres.

For figure 9, the small bump size is varied. Increasing the size of the small bumps reduces the possibility of loss of contact (stage LC) and of simultaneous contact via the small bumps and a large bump (stage CSL). For example, there is no loss of contact with the first large asperity for $\xi_S = 0.024$ in figure 9 before the small bumps are encountered, whereas there is loss of contact with the first large asperity for $\xi_S = 0.002$ and 0.008 (figure 8) before the small bumps are encountered. However, when the spheres are descending from the second large asperity for $\xi_S = 0.024$ in figure 9, loss of contact is predicted because the angle θ is much larger than when the spheres descended from the first larger asperity and so the normal component of gravity is smaller. Reducing the size of the small bumps also gives other interesting results. For $\xi_S = 0.002$, after the spheres experience the period of descending from the first large bump and then briefly losing contact (LC), they next make contact via a second large bump (stage CL) instead of via the small bumps (stage CS). Because the normal component of the contact force at the second large bump drives the heavy sphere to rotate clockwise, the spheres descend from this second large bump back toward the small bumps between the first and second large bumps ($\mathrm{d}\beta_1/\mathrm{d}t = \omega_1 - \omega > 0$), rather than ascending over or sticking to the second large bump. Just after the first point CL for $\xi_S = 0.002$, the heavy sphere shows a slightly higher rotational velocity than does the line of centres, until point CSL is reached. When contact via both the small bumps and a second large bump occurs (point CSL), the spheres are still not able to rotate over the second large bump, and the heavy sphere rotates with the same rotational speed as the line of centres. Then, the spheres rotate together with slipping ($\omega = \omega_1 \neq \omega_2$) until the tangential component of gravity is sufficiently large for the heavy sphere to rotate over the second large bump (the second point CL), after which the heavy sphere again rotates slower than the line of centres.

Decreasing the angle between the two adjacent large bumps has a similar effect to increasing the size of the large asperities. Figure 10 shows that changing the value of Φ_L strongly affects the occurrence of contact via small bumps. When $\Phi_L = 24^\circ$, for which there are 15 large bumps around the equator of the heavy sphere, no contact between the spheres occurs via the small bumps, and the average hydrodynamic separation between the two spheres is higher than for less dense coverage of large bumps. For $\Phi_L = 36^\circ$ (10 large bumps around the equator), contact with small bumps is predicted, and the second large bump is not encountered until the line of centres has rotated to a sufficiently large angle that the heavy sphere is able to rotate over the second large bump (stage CL) without simultaneously remaining in contact with the small asperities (stage CSL, which is present in figure 6 for $\Phi_L = 30^\circ$).

Figure 11 shows the dimensionless hydrodynamic separation and the angle between the line of centres and the line connecting the centre of the heavy sphere and a large bump versus the angle between the line of centres and vertical, with $\beta_0 = 0^\circ$, -5°, -10°, -15°, -20° and -25°. The other conditions are the same as in figure 6. Variation of β_0 gives rise to changes in the initial contact position relative to a large bump. Since $\Phi_L = 30^\circ$, $\beta_0 = -15^\circ$, -20° and -25° are the same as $\beta_0 = 15^\circ$, 10° and 5°, respectively, and represent cases where the closest large bump is located clockwise from the initial contact point. The initial separation initially decreases with decreasing the β_0 until $\beta_0 = -15^\circ$, for which the two spheres first contact via the small bumps, and then it increases with further decrease of β_0. Figure 11 also shows that, except for

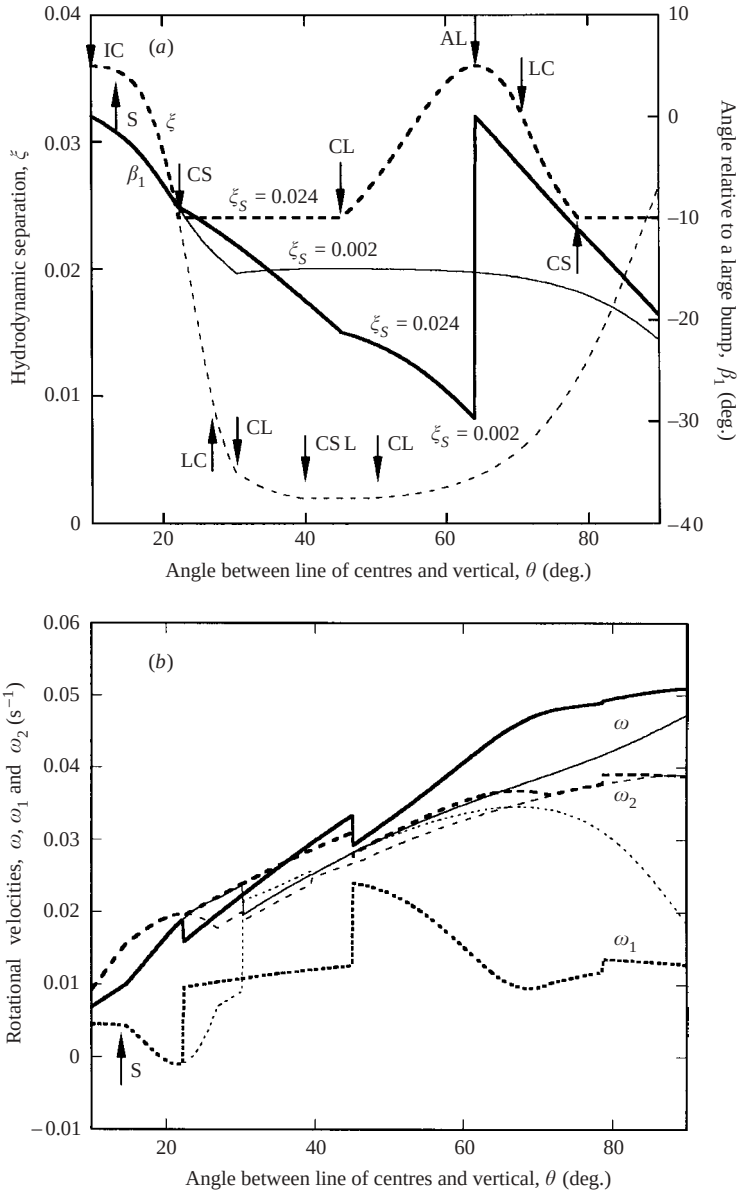

FIGURE 9. Effect of varying the small bump height on (*a*) the dimensionless hydrodynamic separation (dashed lines) and the angle between the line of centres and the line connecting the centre of the heavy sphere and a large bump (solid lines) and (*b*) the rotational velocities of the heavy (dotted lines) and light (dashed lines) sphere and the line of centres (solid lines) versus the angle between the line of centres and vertical, for the same conditions as in figure 6 except $\mu_f = 0.15$ and $\xi_S = 0.002$ (thin lines) and 0.024 (thick lines). S indicates where slipping begins. The rotational velocity may be made dimensionless by dividing by $u_1^0/a_1 = 0.2\,\mathrm{s}^{-1}$ for the conditions of the experiments.

$\beta_0 = -25°$, the motions for the different values of the initial contact angle β_0 coincide after contact is made with the small bumps and $\theta \approx 35°$. For $\beta_0 = -25°$, contact with the small bumps does not occur, and there is a much higher nominal separation (on average) in this case. Note that $|\beta_0| < \Phi_L$ is required by geometrical constraints.

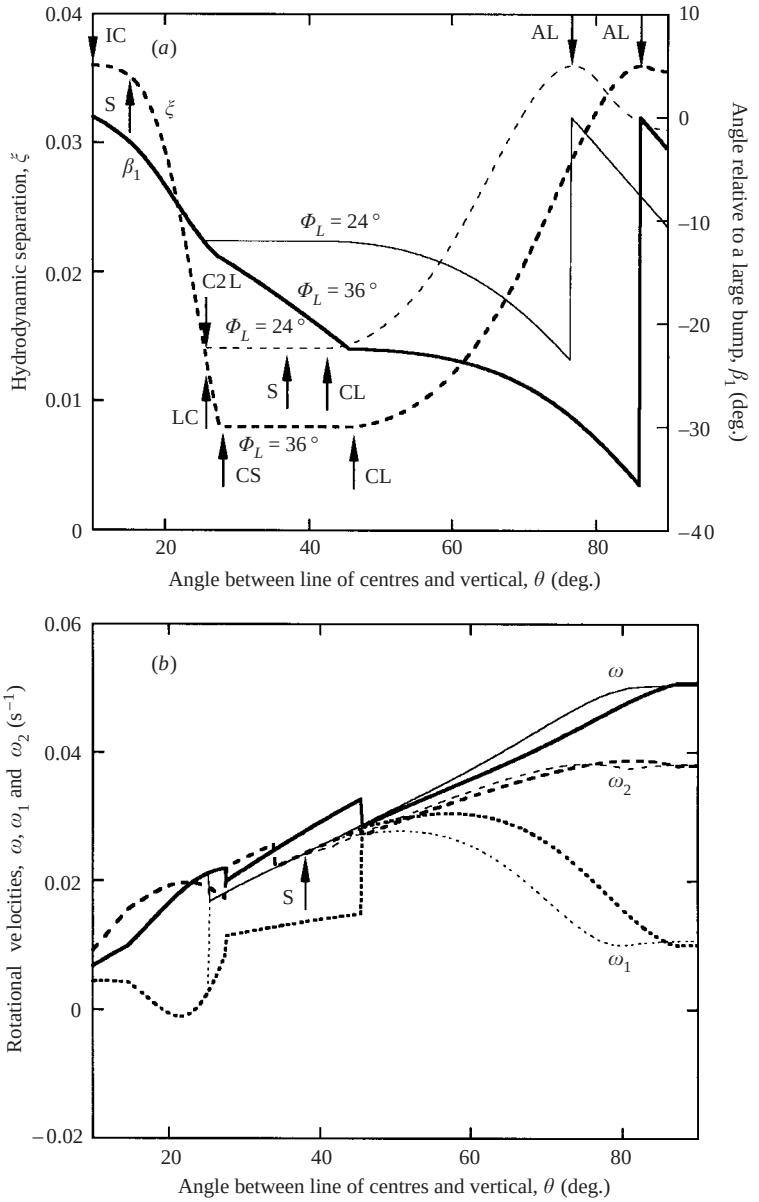

FIGURE 10. Effect of varying the spacing between large bumps on (*a*) the dimensionless hydrodynamic separation (dashed lines) and the angle between the line of centres and the line connecting the centre of the heavy sphere and a large bump (solid lines) and (*b*) the rotational velocities of the heavy (dotted lines) and light (dashed lines) sphere and the line of centres (solid lines) versus the angle between the line of centres and vertical, for the same conditions as in figure 6 but with $\mu_f = 0.15$ and $\Phi_L = 24°$ (thin lines) and 36° (thick lines). S indicates where slipping begins. The rotational velocities may be made dimensionless by dividing by $u_1^0/a_1 = 0.2\,s^{-1}$ for the conditions of the experiments.

In figure 12, the dimensionless hydrodynamic separation and the angle between the line of centres and the line connecting the centre of the heavy sphere and a large bump are plotted versus the angle between the line of centres and vertical, with the initial conditions of $\beta_0 = 0°$ and $\theta_0 = 10°$, 20°, 30°, 40°, 50°, 60° and 70°. The other

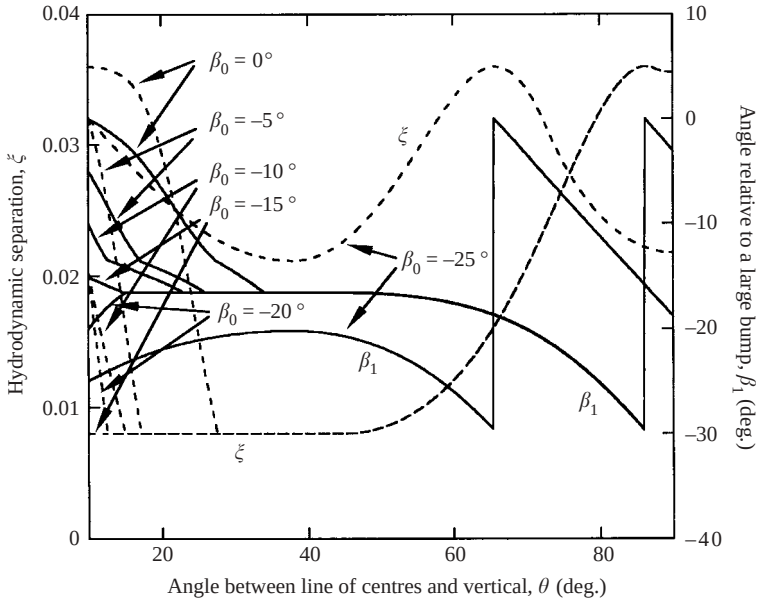

FIGURE 11. Effect of varying the initial contact angle β_1 on the dimensionless hydrodynamic separation (dashed lines) and the angle between the line of centres and the line connecting the centre of the heavy sphere and a large bump (solid lines) versus the angle between the line of centres and vertical, starting from initial conditions of $\theta_0 = 10°$ and $\beta_0 = 0°$, $-5°$, $-10°$, $-15°$, $-20°$ and $-25°$, with $\xi_L = 0.036$, $\xi_S = 0.008$, $\Phi_L = 30°$, $\gamma = 0.02$, $\lambda = 1$ and $\mu_f = 0.15$.

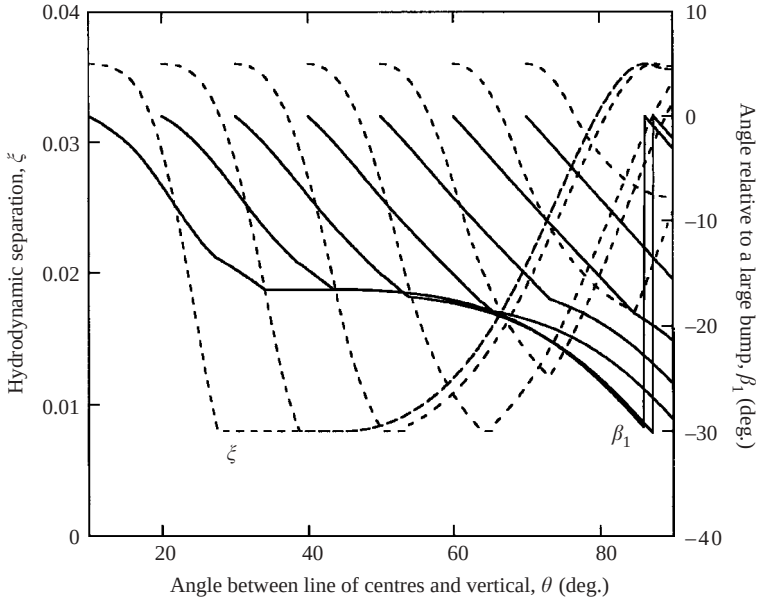

FIGURE 12. Effect of varying the initial contact location θ_0 on the dimensionless hydrodynamic separation (dashed lines) and the angle between the line of centres and the line connecting the centre of the heavy sphere and a large bump (solid lines) versus the angle between the line of centres and vertical, starting from initial conditions of $\beta_0 = 0°$ and $\theta_0 = 10°$, $20°$, $30°$, $40°$, $50°$, $60°$ and $70°$ (left to right), with $\xi_L = 0.036$, $\xi_S = 0.008$, $\Phi_L = 30°$, $\gamma = 0.02$, $\lambda = 1$ and $\mu_f = 0.15$.

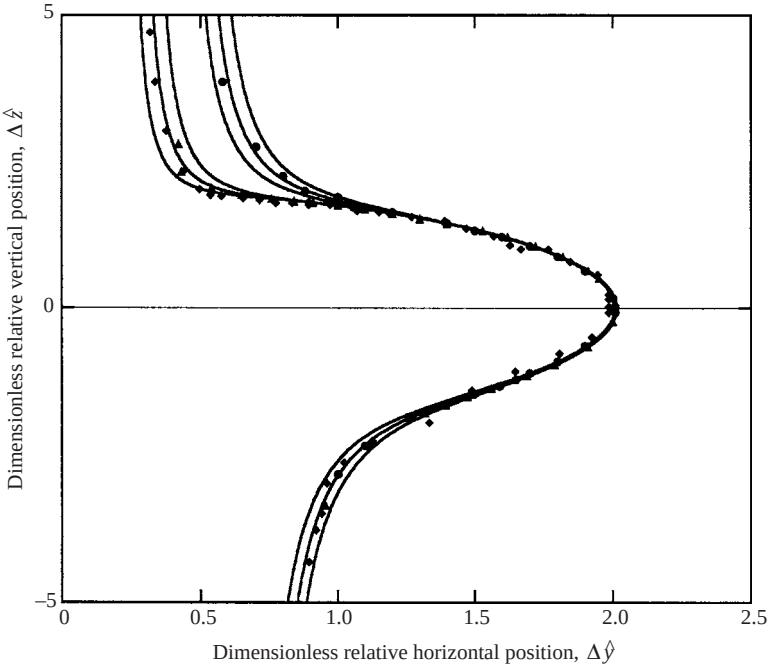

FIGURE 13. Dimensionless trajectories of the centre of a heavy sphere relative to a light one from three experiments (symbols) and theory (curves). The different curves for the upstream parts are calculated with initial dimensionless offsets of $\Delta\hat{y}_0 = 0.24$, 0.28, 0.32, 0.44, 0.48 and 0.52 (left to right), whereas those for the downstream part are for dimensionless roughness heights of $\xi = 0.028$, 0.036 and 0.044 (left to right).

parameter values are the same as in figure 6. The ascent of the second large bump is similar for all $\theta_0 < 30°$. With increasing θ_0, representing the angle at which contact is first made, the period of contact via the small bumps decreases and then disappears for $\theta_0 > 46°$. This result is because the normal component of gravity (which drives the spheres together) decreases as θ increases. A practical consequence is that the average separation is expected to be dominated by the size of the large bumps as the line of centres approaches horizontal.

5. Experimental results

Figure 13 shows the relative trajectories of the centre of a heavy sphere relative to a light one for three different experiments. The top part of each trajectory is only affected by the initial horizontal separation between the centres of the two spheres, whereas the bottom part depends on the dimensionless nominal separation between the spheres when they first separate at $\theta = 90°$. In figure 13, the best-fit of the experimental data for the upper parts of the trajectories give $\Delta\hat{y}_0 = 2\Delta y_0/(a_1 + a_2) = 0.26$, 0.28 and 0.48, for three experiments with different initial offsets. The best-fit of the experimental data for the lower parts give $\xi \approx 0.036$ at $\theta = 90°$ for all three experiments. This result corresponds to a dimensionless value of $\delta = 115\,\mu$m, which is close to the size of the beads that form the large bumps. Consistent with theory (e.g. figure 11), the nominal separation at $\theta = 90°$ is dominated by the size of the large asperities, even though they are sparsely distributed, and it is not very sensitive to the initial angles when contact first occurs.

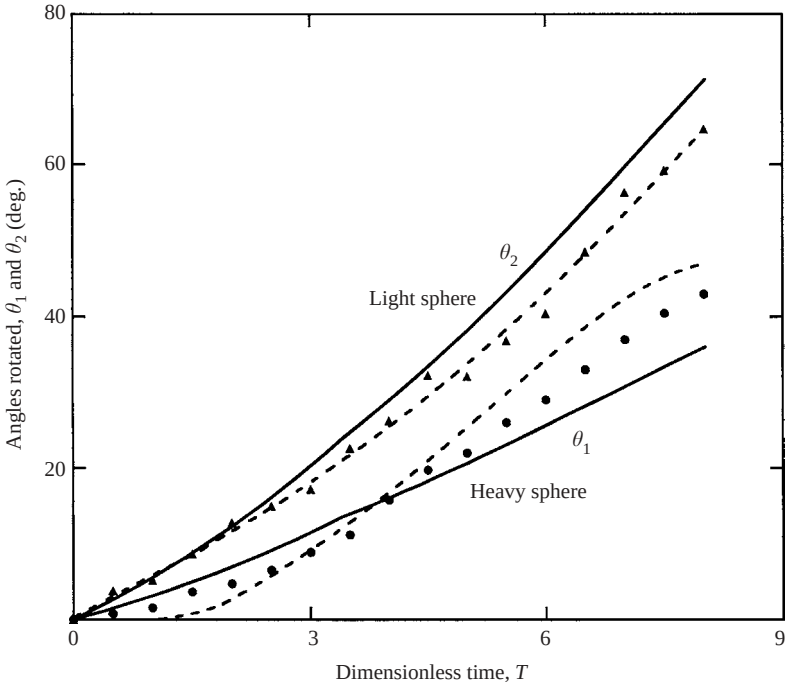

FIGURE 14. The angles through which the heavy and light spheres rotated versus dimensionless time from experiment (symbols) and theory (curves) for the roll/slip model with one bump height (solid lines) and the current model for two bump heights (dashed lines) The conditions are $\theta_0 = 20°$, $\beta_0 = -6°$, $\xi_L = 0.036$, $\xi_S = 0.0057$, $\Phi_L = 20°$, $\gamma = 0.02$, $\lambda = 1$ and $\mu_f = 0.15$. For the model with one bump height, results are shown for $\xi = 0.0057$.

In figure 14, the results for the experiment with $\Delta\hat{y}_0 = 0.28$ in figure 13 are compared with the theoretical solutions for both the roll/slip model with one bump size (solid lines) and the current model with two bump sizes (dashed lines). For this experiment, the light sphere shows a greater rotation rate than the heavy sphere, especially for short times. Therefore, the initial contact stage of the two spheres is that of descending from a large bump ($\beta_0 < 0°$), so that the torque exerted on the heavy sphere by the normal component of the contact force slows its clockwise rotation. The value $\beta_0 = -6°$ was selected to provide the best model fit of the experimental data. For later times, a second large bump is encountered, and the rotational velocity of the heavy sphere increases as it ascends the second large bump, due to the torque exerted by the contact force now aiding its motion. For the light sphere, because the normal component of the contact force always passes through its centre and provides no torque, the rotation shows only a slight difference between the model with a single bump size and the model with two bump sizes.

Figure 15 shows the comparison of the experimental results for the dimensionless hydrodynamic separation with the model predictions, averaged over a random distribution of all possible initial angles β_0, versus the angle θ between the line of centres and vertical. The different solid lines are for contact first occurring at $\theta_0 = 5°$, 10°, 10°, 30°, 40°, 50°, 60° and 70° (left to right), whereas the dashed lines are the results averaged over all $0 < \theta_0 < \theta$. In these experiments, the heavy sphere started with a random placement above the light sphere and then fell until contact was made at initial angles β_0 and θ_0, which varied from run to run. The heavy sphere then moved

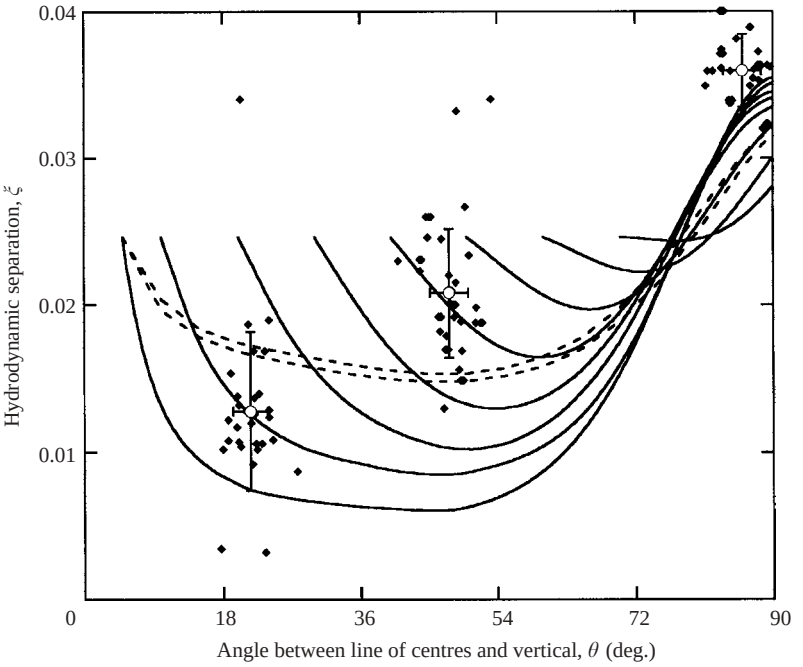

FIGURE 15. Comparison of theoretical (curves) and the experimental (symbols) results for the dimensionless hydrodynamic separation versus the angle between the line of centres and vertical. The solid curves are model predictions starting from the initial conditions of $\theta_0 = 5°$, 10°, 20°, 30°, 40°, 50°, 60°, and 70° (left to right), averaged over all initial β_0, with $\xi_L = 0.036$, $\xi_S = 0.0057$, $\Phi_L = 29°$, $\gamma = 0.02$, $\lambda = 1$ and $\mu_f = 0.25$. The dashed lines are the overall average separation from equation (5.1) with $\xi_S = 0.0057$ (top) and $\xi_S = 0.0034$ (bottom). The error bars represent $\pm$ one standard deviation for multiple experiments (29 with $\theta \approx 22°$, 43 with $\theta \approx 48°$, 49 with $\theta \approx 86°$).

around the surface of the light sphere until an angle θ was reached. At this point, the container was inverted, so that the heavy sphere was directly below the light sphere, and the nominal separation was determined from (3.2) based on measurements of the time it took the heavy sphere to fall to a given separation from the light sphere. While the initial orientation angle β_0 for the nearest large bump is randomly distributed, the distribution of the initial contact angle θ_0 has a weight factor of $\sin\theta_0 \cos\theta_0$, based on the probability of a particle pair making initial contact at the angle θ_0 given a random initial placement of the heavy sphere far above the light sphere. The factor $\sin\theta_0$ comes from the area of a ring-shaped surface element at the angle θ_0, and the factor of $\cos\theta_0$ comes from the normal component of the relative velocity of the two spheres due to the component of the gravitational force acting along the line of centres. Note that the particle pair probability, for a random distribution when well separated, is independent of the angle θ_0 (Batchelor 1982). Thus, the dashed line in figure 15 is the overall average given by

$$\langle \xi(\theta) \rangle = \frac{\displaystyle\int_0^{\theta} \int_{-\phi_L}^{0} \xi(\theta; \beta_0, \theta_0)\, \mathrm{d}\beta_0 \sin\theta_0 \cos\theta_0\, \mathrm{d}\theta_0}{(\Phi_L \sin^2\theta)/2}. \tag{5.1}$$

Both the data and theory in figure 15 show a broad distribution of the nominal separation between the sphere surfaces, especially at small and moderate values of the

angle θ, due to the multiple roughness scales. A primary finding from figure 15 is that the average separation generally increases with increasing angle θ, becoming nearly equal to the height of the large bumps ($\xi_L = 0.036$) as the line of centres becomes horizontal ($\theta = 90^\circ$). This result occurs because an encounter with a large bump causes the spheres to lift away from each other to a dimensionless separation ξ_L, and the component of gravity which pushes them back together becomes weaker as the particle pair rotates toward horizontal. The observation that many of the measured separations are slightly higher than the predicted values as $\theta \to 90^\circ$ is probably due to the presence of natural surface roughness on the light sphere that is not included in the model. In contrast, we note that the average measured separation falls below the average predicted separation at the smallest angles examined ($\theta \approx 22^\circ$). In the model predictions for these angles, the initial contact with a large asperity plays a large role, as the decrease in the nominal separation from a large bump to the small bumps is slowed by the lubrication resistance. Moreover, the model is restricted to axisymmetric motion, with the large asperities projected onto the equator of the heavy sphere. In the experiments, however, a large asperity may be encountered which is to one side of the equator. Then, the heavy sphere will not roll directly over this bump but instead it will also tip sideways, which reduces the nominal separation.

Finally, the lower and upper dashed lines are for $\xi_L = 0.0034$ ($\delta_S = 10\,\mu\text{m}$) and $\xi_S = 0.0057$ ($\delta_S = 18\,\mu\text{m}$), corresponding to the small bump height equal to the natural roughness of the teflon sphere and to the sum of natural roughnesses of the teflon and nylon spheres, respectively. Clearly, the variation of the small bump size in this range has little effect on the overall results.

6. Concluding remarks

This work has examined the contact and near-contact interaction of two unequal spherical particles with multiscale surface roughness, sedimenting due to gravity at low Reynolds number in a viscous fluid of large extent. Even with microscopic surface asperities of only two sizes, the behaviour is considerably more complex than for interactions with a single roughness scale. The influence of microscopic roughness on the rotational motion of one sphere past the other is expected to affect the rheological behaviour of a sheared suspension (Wilson & Davis 2000, 2002), in addition to the separation of species of different sizes or densities in gravitational sedimentation.

Following previous work, the model assumes that the roughness elements are sufficiently small and sparse that they do not affect the hydrodynamic interactions of the spheres. The physical contact (which is prevented by lubrication forces for smooth spheres) occurs when the nominal separation decreases to the local roughness height as a heavy sphere falls downward onto a lighter (or smaller) sphere. The heavy sphere will roll and possibly slip around the surface of the light sphere in contact with the smaller bumps until a larger bump is encountered. If the latter asperity is sufficiently tall, and the angle between the gravity vector and the line of centres is sufficiently small, then the heavy sphere will not be able to pivot over this tall bump and so the two spheres will rotate together in rigid-body motion or, for small friction, the heavy sphere will slide without rolling around the surface of the light sphere. Eventually, the line of centres will rotate to where the component of gravity perpendicular to this line is sufficiently large that the heavy sphere rotates up and over the tall bump. The heavy sphere is then driven back toward the light sphere by the component of gravity parallel to the line of centres. However, as the angle between the line of centres and the vertical increases during the interaction, the component of gravity along the line of

centres becomes weaker and so the nominal separation tends to remain close to the height of the large asperities. Indeed, both theory and experiment show that the nominal surface-to-surface separation when the line of centres approaches horizontal is essentially equal to the large bump height, independent of the conditions where contact first occurs. Since rheological information such as the pair-distribution function and hydrodynamic diffusion in dilute suspensions is dependent on the two-sphere trajectories after contact ends, once the pair becomes horizontal the large bumps can have a dominant effect.

In contrast, the nominal surface separation at moderate angles between the line of centres and vertical tends to be much closer to the height of the small asperities, aided by the period when the two spheres make contact simultaneously via the small bumps and a large bump and are not able to pivot over the large bump. At small angles, there is a large variation in the nominal separation and in the rotational motion of the spheres, with a strong dependence on bump sizes and locations and on the initial contact location.

The experiments support the model predictions, except that the nominal surface separation measured experimentally is smaller, on average, than that predicted by the model when the angle between the line of centres and vertical is small. It is thought that this difference is caused by sideways tipping of the spheres off a large asperity in the experiments, which is not accounted for in the axisymmetric model. Exploration of fully three-dimensional interactions during particle–particle contacts, and of surface topologies with many roughness heights and spatial distributions, may be of interest in future work.

This work was supported by the National Science Foundation through grant CTS-9712604 and by the National Aeronautics and Space Administration through grant NCC3-796.

REFERENCES

Arp, A. P. & Mason, S. G. 1977 The kinetics of flowing dispersions. IX. Doublets of rigid spheres (experimental). *J. Colloid Interface Sci.* **61**, 44–61.

Batchelor, G. K. 1982 Sedimentation in a dilute polydisperse system of interacting spheres. Part 1. General theory. *J. Fluid Mech.* **119**, 379–408.

Batchelor, G. K. & Wen, C. S. 1982 Sedimentation in a dilute polydisperse system of interacting spheres. Part 2. Numerical results. *J. Fluid Mech.* **124**, 495–528.

da Cunha, F. R. & Hinch, E. J. 1996 Shear-induced dispersion in a dilute suspension of rough spheres. *J. Fluid Mech.* **309**, 211–223.

Davis, R. H. 1992 Effects of surface roughness on a sphere sedimenting through a dilute suspension of neutrally buoyant spheres. *Phys. Fluids* A **4**, 2607–2619.

Galvin, K. P., Zhao, Y. & Davis, R. H. 2001 Time-averaged hydrodynamic roughness of a noncolloidal sphere in low Reynolds number motion down an inclined plane. *Phys. Fluids* **13**, 3108–3119.

Jeffrey, D. J. & Onishi, Y. 1984 Calculation of the resistance and mobility functions for two unequal rigid spheres in low-Reynolds-number flow. *J. Fluid Mech.* **139**, 261–290.

King, M. R. & Leighton, D. T. 1997 Measurement of the inertial lift on a moving sphere in contact with a plane wall in shear flow. *Phys. Fluids* **9**, 1248.

Parsi, F. & Gadala-Maria, F. 1987 Fore-and-aft asymmetry in a concentrated suspension of solid spheres. *J. Rheol.* **31**, 725–732.

Prokunin, A. N. 1998 Spherical particle sedimentation along an inclined plane at small Reynolds numbers. *Fluid Dyn.* **23**, 573–579.

Rampall, I., Smart, J. R. & Leighton, D. T. 1997 The influence of surface roughness on the particle-pair distribution function of dilute suspensions of non-colloidal spheres in simple shear flow. *J. Fluid Mech.* **339**, 1–24.

Reynolds, O. 1886 On the theory of lubrication and its application to Mr. Beauchamp Tower's experiments. *Phil. Trans. R. Soc. Lond.* A **177**, 157–234.

Smart, J. R., Beimfohr, S. & Leighton, D. T. 1993 Measurement of the translational and rotational velocities of a noncolloidal sphere rolling down a smooth inclined plane at low Reynolds number. *Phys. Fluids* A **5**, 13–24.

Smart, J. R. & Leighton, D. T. 1989 Measurement of the hydrodynamic surface roughness of noncolloidal spheres. *Phys. Fluids* A **1**, 52–60.

Wilson, H. J. & Davis, R. H. 2000 The viscosity of a dilute suspension of rough spheres. *J. Fluid Mech.* **421**, 339–367.

Wilson, H. J. & Davis, R. H. 2002 Shear stress of a monolayer of rough spheres. *J. Fluid Mech.* **452**, 425–441.

Zeng, S., Kerns, E. T. & Davis, R. H. 1996 The nature of particle contacts in sedimentation. *Phys. Fluids* **8**, 1389–1396.

Zhao, Y. & Davis, R. H. 2002 Interaction of two touching spheres in a viscous fluid. *Chem. Engng Sci.* **57**, 1997–2006.

Zhao, Y., Galvin, K. P. & Davis, R. H. 2002 Motion of a sphere down a rough plane in a viscous fluid. *Intl J. Multiphase Flow* **28**, 1787.